Petroleum Science 23 (2026) 2002–2016

Contents lists available at ScienceDirect

Petroleum Science

journal homepage: www.keaipublishing.com/en/journals/petroleum-science

Original Paper

# Supramolecular polymer gels reinforced by cellulose nanofibers and laponite for lost circulation control of fractured oil and gas reservoirs

Li-Yao Dai [a], Jin-Sheng Sun [a,c], Kai-He Lv [a,c], Ying-Rui Bai [a,c], Bo Liao [a], Dong-Qing Yang [a], Chao-Zheng Liu [b], Mei-Chun Li [a,c,d,*]

[a] School of Petroleum Engineering, China University of Petroleum (East China), Qingdao, 266580, Shandong, China
[b] Co-Innovation Center of Efficient Processing and Utilization of Forest Resources, College of Materials Science and Engineering, Nanjing Forestry University, Nanjing, 210037, Jiangsu, China
[c] State Key Laboratory of Deep Oil and Gas, China University of Petroleum (East China), Qingdao 266580, Shandong, China
[d] Shandong Key Laboratory of Oil and Gas Field Chemistry, China University of Petroleum (East China), Qingdao, 266580, Shandong, China

ARTICLE INFO

*Article history:*
Received 9 July 2025
Received in revised form
12 December 2025
Accepted 24 December 2025
Available online 30 December 2025

Edited by Yan-Hua Sun

*Keywords:*
Fractured reservoir
Lost circulation material
Supramolecular polymer gel
Cellulose nanofiber
Laponite

ABSTRACT

Fractures in geological formations, which are commonly encountered during oil and gas exploration, pose significant challenges by facilitating fluid loss and reducing wellbore stability. Polymer gels hold significant promise as lost circulation materials due to their excellent deformability under pressure and self-adaptability. However, conventional gels face certain limitations, such as poor retention of gel-forming suspensions in fractures, low structural strength, and instability at high temperatures. These issues result in low pressure-bearing capacity and, consequently, reduced effectiveness in sealing formation fractures. This study presents the synthesis of a supramolecular polymer gel (SPG) composed of acrylamide (AM), 2-acrylamide-2-methylpropanesulfonic acid (AMPS), divinylbenzene (DVB), polyvinyl alcohol (PVA), TEMPO-oxidized cellulose nanofibers (CNFs), and laponite via in situ radical polymerization. Due to the synergistic effects of hydrogen bonding and electrostatic interactions, the supramolecular polymer gel-forming suspension exhibits high retention capacity in fractures. The as-synthesized gels demonstrate remarkable temperature resistance and high mechanical strength, attributed to covalent bonding, multiple hydrogen bonding, and electrostatic interactions, along with the high aspect ratio and modulus of CNFs and laponite. This study broadens the application scope of CNFs, laponite, and SPGs, offering a novel approach for the efficient development of unconventional oil and gas resources.



## 1. Introduction

In the contemporary global energy landscape, unconventional oil and gas resources—such as heavy oil, tight oil, shale gas, and coalbed methane—are pivotal for safeguarding energy security and transforming energy structures, owing to their substantial reserves and promising development prospects (Wang et al., 2016; Zheng et al., 2017). However, compared with conventional reservoirs, unconventional ones are typically characterized by ultra-low permeability, strong heterogeneity, and complex pore-fracture systems (Chen et al., 2019; Dai et al., 2025a; Han et al., 2025; Tao et al., 2024). Therefore, their economic development necessitates advanced drilling technologies (Song et al., 2017).

Lost circulation is a complex downhole challenge where various working fluids infiltrate the formation through pores and fractures due to pressure differentials during operations such as drilling, cementing, completion, testing, or workover (Guo et al., 2024a). In drilling engineering, lost circulation specifically refers to the phenomenon where drilling fluids leak into the formation during drilling. This issue not only leads to significant fluid loss and increased drilling costs but also contributes to a series of complex downhole problems, such as wellbore instability and stuck pipe, which severely disrupt the smooth progression of drilling operations (Kang et al., 2023; Xu et al., 2020, 2023).

* Corresponding author.
*E-mail address:* mli@upc.edu.cn (M.-C. Li).
Peer review under the responsibility of China University of Petroleum (Beijing).

https://doi.org/10.1016/j.petsci.2025.12.037

Therefore, effectively addressing drilling fluid leakage is critical to ensuring the safety and efficiency of drilling engineering.

Among the various methods to mitigate lost circulation, the use of lost circulation materials to seal fractures is one of the most widely employed approaches (Lin et al., 2024). Common lost circulation materials include bridging materials, chemical polymer gels, and inorganic gels (Guo et al., 2024; Nasiri et al., 2018; Su et al., 2019; Zhang et al., 2022). Bridging materials, typically composed of inert granular, fibrous, and flake materials blended in specific mass ratios and particle size distributions, offer advantages such as minimal impact on drilling fluids, low cost, and ease of operation (Lin et al., 2022). However, the effectiveness of bridging materials heavily depends on their concentration and particle size gradation. Chemical lost circulation materials, particularly polymer gel-based systems, exhibit excellent adaptability and deformability in fractures, unaffected by fracture geometry (Guo et al., 2024b; Zhou et al., 2024). However, conventional polymer gels often lack sufficient sealing strength and temperature resistance in fractures. Inorganic gels, primarily cement-based, possess high pressure-bearing capacities after curing and are cost-effective due to their abundant availability (Aslani et al., 2022; Li et al., 2024a; Xu et al., 2024c). Yet, these materials are prone to dilution by formation water, and their curing time and rate are difficult to control. As exploration and production depths increase, conventional lost circulation materials struggle to meet the demands of complex working environments, demanding the design of high-strength, high-performance alternatives.

In recent years, supramolecular polymer gels (SPGs), with their physical and chemical properties, have shown great promise in the field of lost circulation materials. SPGs contain three-dimensional network structures that are multifunctional, reversible, and stimulus-responsive (Appel et al., 2012; Huang et al., 2022b). These materials exhibit distinct properties, such as tunable rheology and excellent adaptability, making them inherently advantageous for sealing fractures. Among SPGs, those based on polyvinyl alcohol (PVA) have attracted significant attention due to their abundant hydroxyl group, high strength, superior processability, and outstanding environmental compatibility (Bercea, 2024; Sun et al., 2024). For example, Song et al. (2024) prepared a re-crosslinkable granular gel using PVA, acrylamide, and L-lysine monohydrochloride, achieving a gel expansion ratio of 10 and a modulus of 477 Pa, which was measured at a frequency of 1 Hz and a controlled strain of 1%. Moreover, gel properties were evaluated at 130 °C over 4 d, with a water flooding flow rate of 0.5 mL/min. It was observed that this gel effectively sealed fractures, achieving a water breakthrough pressure gradient of 70 psi/ft for a 3 mm fracture. However, the low mechanical properties and poor thermal stability of PVA-based gels constrain their broader application (Adelnia et al., 2022; Maiolo et al., 2012; Zhao et al., 2024). Consequently, improving the thermal and mechanical performance of SPGs remains a critical focus of current research.

The integration of nano-additives into SPGs has gained attention as a strategy to enhance the performance of SPGs. Cellulose nanofibrils (CNFs), a promising cellulose derivative, possess a high aspect ratio and abundant hydroxyl groups, which facilitate the creation of three-dimensional networks within SPGs at low concentrations (Kang et al., 2023; Zhu et al., 2024). CNFs also exhibit excellent shear-thinning behavior, making them ideal for enhancing the retention capacity of gel-forming suspension in fractures (Li et al., 2015, 2021). For example, Yang et al. (2023) fabricated a blended gel matrix temporary plugging agent using TEMPO-oxidized CNFs, polyacrylamide, and polyethyleneimine. The rheological properties were measured at a fixed frequency of 1 Hz, and the CNF-reinforced gel exhibited a 1332% increase in elastic modulus compared to gels without CNFs. Similarity, Li et al. (2022) prepared CNF-reinforced poly(acrylamide-co-acrylic acid) hydrogel. Mechanical tests were conducted on cylindrical samples (16 mm in diameter and 20 mm in thickness) at room temperature, with a compression speed of 20 mm/min, and up to 90% of the maximum compressive strain. A sevenfold improvement in compressive strength was achieved by incorporating 0.2 wt% CNFs. Liu et al. (2023) introduced CNFs and $Fe^{3+}$ into a SPG system consisting of polyacrylic acid. Mechanical properties were measured using samples 50 mm in length and 4 mm in diameter, at room temperature and a tensile rate of 20 mm/min. The CNF-filled SPG exhibited a stress of 1.03 MPa and a high strain of 1491%. These studies highlight the significant potential of CNFs as reinforcing fillers in supramolecular gels for sealing agent applications. Furthermore, in our previous research, a SPG for the temporary plugging of fractured oil and gas reservoirs was successfully prepared (Dai et al., 2025b). This system demonstrated promising results in enhancing gel properties and fulfilling the requirements for temporary plugging applications. However, as exploration advances into increasingly complex geological formations, the performance demands for lost circulation materials have intensified. Key challenges now include enhancing the retention of gel-forming suspensions within fractures, improving sealing strength after gelling, and ensuring adequate temperature resistance.

The incorporation of clay nanoparticles into SPGs offers significant enhancements in their rheological, mechanical, and thermal properties (Li et al., 2017; Zhao et al., 2015). Laponite is a synthetic, layered silicate nanoclay composed primarily of sodium magnesium lithium silicate, known for its high surface area and thixotropic properties. It is widely used in applications such as rheology control, gel formation, and as a template or additive in advanced materials due to its unique colloidal behavior and tunable interactions in aqueous systems. Its layered structure, intrinsic surface charges, and rheological versatility contribute to improved mechanical strength, thermal stability, and interfacial interactions within polymer matrices, making it a valuable component in lost circulation material (Li et al., 2024b; Lin et al., 2024; de Oliveira et al., 2015). Therefore, the synergistic combination of CNFs and laponite is anticipated to significantly elevate the performance of supramolecular gels, enhancing their fracture-sealing capability and durability in reservoir applications.

In this study, a SPG was synthesized using acrylamide (AM), 2-acrylamide-2-methylpropanesulfonic acid (AMPS), divinylbenzene (DVB), polyvinyl alcohol (PVA), TEMPO-oxidized cellulose nanofibrils (CNFs), and laponite via in situ radical polymerization. Owing to component synergism, the synthesized gel displayed remarkable load-bearing capability and excellent high-temperature resistance. Due to the incorporation of double bonds and aromatic structures in the copolymerized monomers, the gels exhibit improved strength and heat resistance. Moreover, the synergistic non-covalent interactions among PVA chains, cellulose nanofibrils, and laponite contributed to additional enhancement of the gel's overall performance. Finally, CNFs and laponite also served as reinforcing additives and rheological modifiers in the polymer, these changes improved three key aspects: physical properties, thermal stability, and thixotropic properties of the suspension. Consequently, the resulting gel demonstrated a compressive strength of 0.169 MPa at 75% compressive strain, a core sealing strength of 16 MPa, and thermal aging resistance up to 120 °C for 30 d.

## 2. Experimental section

### 2.1. Materials

Aladdin supplied polyvinyl alcohol (PVA), 2-acrylamido-2-methylpropanesulfonic acid (AMPS), acrylamide (AM, purity

>98%), ammonium persulfate (APS), and divinylbenzene (DVB). TEMPO-oxidized cellulose nanofibers (CNFs, with a solid content of 2.6 wt%) were provided by Shenquan Group Co. Ltd., Jinan, China. laponite ($Li_2Mg_2O_9Si_3$, average diameter: 25–30 nm, thickness: 1 nm) was kindly supplied by Lanabai Pharmaceutical Chemical Co., Wuhan, China.

### 2.2. Synthesis of gels

PVA was dissolved in water at 95 °C. After the solution was cooled, AM, AMPS, DVB, reinforcing materials, and resin-coated initiators were added sequentially and stirred thoroughly to form the gels. The specific concentrations are listed in Table S1. The SPG samples prepared with 0 wt% CNFs, 0.30 wt% CNFs, 3 wt% laponite, and a combination of 0.30 wt% CNFs and 3 wt% laponite are referred to as SPG-N, SPG-C, SPG-L, and SPG-B, respectively.

### 2.3. Characterization

#### 2.3.1. Fourier transform infrared spectroscopy (FTIR)

FTIR spectra of the gels were acquired using an IRTracer-100 spectrometer (Shimadzu, Japan). The wavelength ranged from 500 to 4000 $cm^{-1}$.

#### 2.3.2. Scanning electron microscopy (SEM)

The morphology of the freeze-dried gel samples was observed using a ZEISS Sigma 360 scanning electron microscope and an Oxford Ultim Max 40 spectrometer (Germany). Prior to imaging, the samples were lyophilized at −60 °C overnight and sputter-coated with a thin gold layer.

#### 2.3.3. X-ray diffraction (XRD)

The crystallinity of the gels was analyzed using a Bruker D8 QUEST diffractometer (Germany) with scanning conducted over a $2\theta$ range of 5°–70°.

#### 2.3.4. X-ray photoelectron spectroscopy (XPS)

XPS measurements were carried out on a Thermo Scientific ESCALAB Xi + spectrometer with an Al-K X-ray source (1486.6 eV).

#### 2.3.5. Mechanical properties

Tensile and compression strengths were measured using a universal testing machine (Xie LiLing Instrument Manufacturing Co. Ltd., Shandong, China) at a tensile speed of 50 mm/min and a compression speed of 20 mm/min, respectively.

#### 2.3.6. Rheological properties

Dynamic rheological properties were evaluated using a HAAKE MARS 60 rheometer (Thermo Fisher Scientific, Germany) with a P35 Ti L plate (diameter: 35 mm). Frequency sweeps were conducted at 25 °C, with a strain of 10% and frequencies ranging from 0.5 to 84 rad/s. Thixotropic behavior was analyzed at a fixed stress of 10 Pa through oscillatory strain cycles (10%–200%–10%). Flow behavior was assessed using the same rheometer with a CC41 Ti cylinder (diameter: 41 mm). Shear stress and viscosity were measured across shear rates of 0.1–100 $s^{-1}$ at 25 °C.

#### 2.3.7. Adhesive performance

Adhesion between the suspension and quartzite cores was evaluated using a Dataphysics tensiometer (Dataphysics Ltd., Germany).

#### 2.3.8. Fracture filling performance

A fracture board apparatus was used to visualize gel-forming suspension filling in wedge-shaped and parallel fractures under controlled conditions. Two distinct fracture models, a wedge-shaped fracture and a parallel fracture, were specifically developed and constructed for this purpose. The wedge-shaped model measured 25 cm in length, 5.5 cm in width, and had a height varying from 3 to 6 mm; while the parallel fracture model measured 35 cm long, 20 cm wide, and had a uniform height of 3 mm. The tilt angle of the model was modified according to requirements, and the solutions were transferred via a flow pump. The fill factor was obtained using the given formula:

$$f = V_1/V_2 \times 100\% \quad (1)$$

where $V_1$ represents the volume occupied by the suspension; $V_2$ represents the initial void volume of the fracture. We measured the dip angle of the suspension in the fracture with a calibrated angle square.

#### 2.3.9. Sealing performance

We evaluated the SPG sealing characteristics in porous media by employing an HTHP (Nantong Xinhuacheng scientific research Instrument Co., Ltd., China) core flooding test system. The device's oven was preheated to 120 °C to simulate the targeted formation temperature. A cylindrical model (45 mm diameter × 20 cm length) was packed with quartz sand (40–80 mesh, with a permeability of (2000–10000) × $10^{-3}$ $\mu m^2$) and placed inside the device.

## 3. Results and discussion

### 3.1. Synthesis and molecular architecture of SPGs

As depicted in Fig. 1(a), the successful synthesis of SPGs was achieved by integrating covalent bonds, multiple hydrogen bonds, and ionic bonds within their molecular structures, creating highly interconnected networks. The monomers selected for this reaction were AM and AMPS, with DVB serving as the crosslinking agent to form the SPG. Comonomer's –CONH– and $–SO_3H$ groups enable strong H-bonding and salt tolerance (Sajjadi et al., 2024; Zheng et al., 2023). The inclusion of DVB, with its benzene ring structure, further enhanced the thermal endurance of the polymer under high-temperature reservoir conditions.

The SPG system was further reinforced via non-covalent bonding. PVA, CNFs, and laponite were incorporated, which contains abundant hydroxyl groups and charges on the surface. Particularly, CNFs exhibit a fiber-like morphology with a high aspect ratio and network-like structure, while laponite shows a disc-shaped morphology with a uniform nanometer-scale thickness (Fig. S1). These additions facilitated the generation of multiple hydrogen bonding within the system (Fig. 1(a)). For instance, H-bonding interactions can be generated not only between CNFs and hydroxyl groups in PVA, but also with –CONH– in the polymer chain (poly(AM-DVB-AMPS)) (Liu et al., 2024; Wei et al., 2024). Furthermore, hydrogen bonding interactions between the Si–OH groups on laponite's surface and hydroxyl groups in PVA and amide groups in poly(AM-DVB-AMPS) significantly increased the number of hydrogen bonding in the SPG (Mahdavinia et al., 2016, 2017).

More importantly, when dispersed in an aqueous solution, laponite formed a three-dimensional network structure, the phenomenon stems from the electrical attraction occurring between anionically charged surface areas and cationic edge locations (Gu et al., 2023; Prasannan et al., 2020). The negatively charged CNFs (i.e., carboxylated group) and poly(AM-DVB-AMPS) (i.e., sulfonated group) interacted with the positively charged edges of laponite (i.e., Mg-$OH_2^+$) through electrostatic attraction, as well.

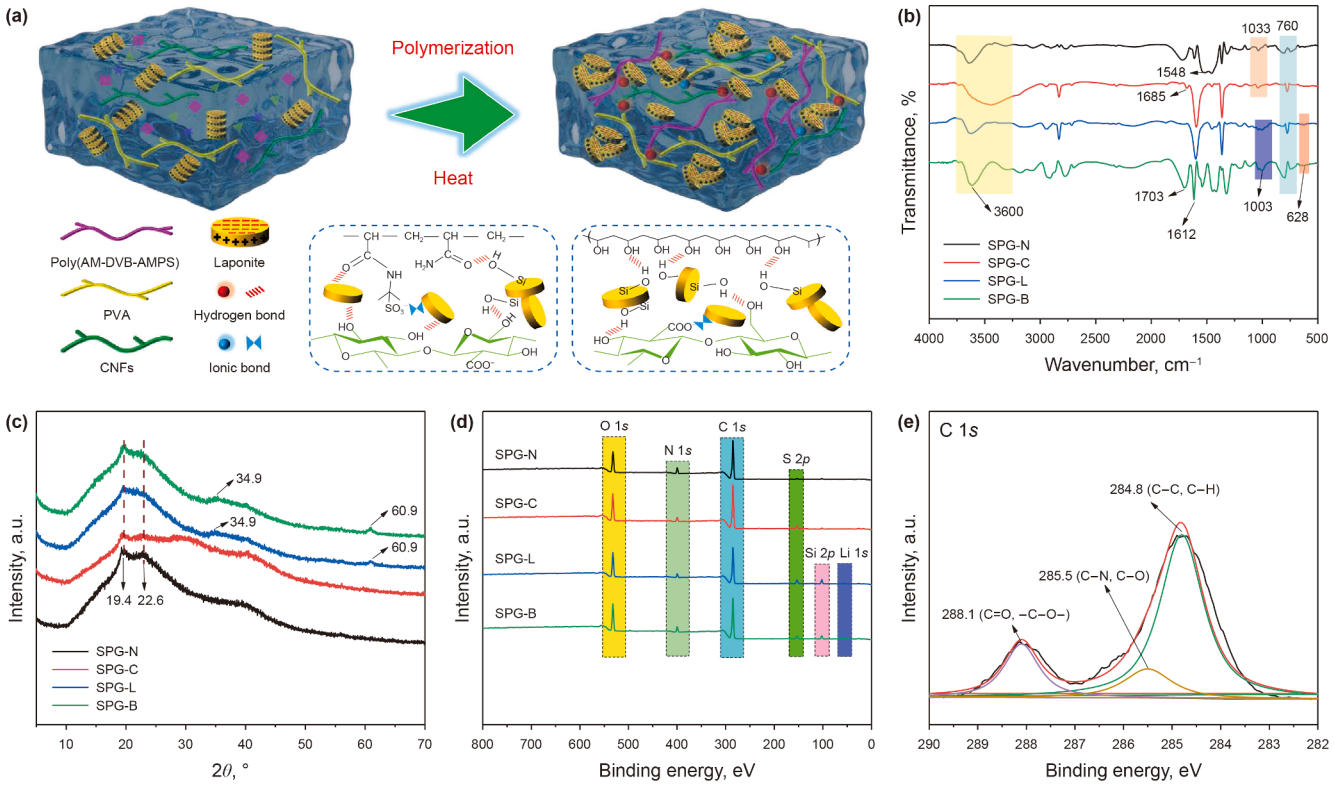


**Fig. 1.** Preparation and characterizations of synthesized gels: (**a**) a schematic representation of the chemical structure and intermolecular interactions within the gels, (**b**) FT-IR, (**c**) XRD, (**d**) XPS, and (**e**) resolved C 1*s* peaks of SPG-B.

These ionic bonds imparted excellent rheological properties to the SPG-forming suspension. Furthermore, the incorporation of CNFs and laponite, with their nano-sized scale, significant length-to-width ratio, and high modulus of elasticity, reinforced the structural integrity of the gels (Lu et al., 2024; Supramaniam et al., 2022; Xu et al., 2024b). Overall, the combination of covalent bond, crosslinking structure, multiple hydrogen bonding, and electrostatic interactions is expected to significantly improve the rheological properties, mechanical strength, and thermal stability of the SPG, leading to superior sealing performance in harsh reservoir condition.

The molecular architectures of the polymer incorporating various reinforcing materials were analyzed via FTIR spectroscopy (Fig. 1(b)). The SPG-N gels exhibited a strong absorption peak at 3300–3650 $cm^{-1}$, resulting from the –OH within the PVA component of the polymer. In addition, identifying features of crosslinked poly(AM-DVB-AMPS) were identified, including the amide group (–C=O–NH–) at 1548 $cm^{-1}$, sulfonic acid group (–$SO_3H$) at 1033 $cm^{-1}$, and the 1,2-diposition substituted aromatic ring at 760 $cm^{-1}$ (Dong et al., 2023). The addition of CNFs (i.e., SPG-C) strengthened H-bonding involving CNFs, PVA, and poly(AM-DVB-AMPS), thereby resulting in a much broader hydroxyl peak. In SPG-L gel, the presence of a peak at 628 and 1003 $cm^{-1}$ was assigned to the Mg–O and Si–O–Si stretching vibrations of laponite (Xu et al., 2024a; Yu et al., 2023). After the addition of CNFs and laponite (i.e., SPG-B), the hydroxyl characteristic peak region shifted to 3427–3705 $cm^{-1}$, demonstrating strong H-bonding interactions between CNFs, laponite, PVA, and poly(AM-DVB-AMPS) (Nezadi et al., 2024). Furthermore, the shift of carboxylic acid absorption peak from 1685 to 1703 $cm^{-1}$ and the merging of sulfonic acid group peak at 1033 $cm^{-1}$ with Si-O-Si group peak at 1003 $cm^{-1}$ in SPG-B indicated the formation of electrostatic interactions among CNFs, laponite, and poly(AM-DVB-AMPS), as well (Bai et al., 2022; Šebenik et al., 2020).

X-ray diffraction (XRD) analysis presents insights into the crystalline structure of the polymer (Fig. 1(c)). SPG-N showed two main XRD peaks positioned at 19.4° and 22.6°, representing the (101) and (200) planes of PVA. SPG-C demonstrated the same diffraction peaks at 12.40° and 20.60°. Notably, the diffraction peaks of CNFs appeared at 12.40° and 20.60°, corresponding to the (110) and (200) crystal planes (Fig. S2(a)), respectively (Silva et al., 2019). The absence of these peaks in SPG-C could be attributed to the relatively low proportion of CNFs (i.e., 0.3 wt%). With respect to SPG-L and SPG-B, two new diffraction peaks were observed at 34.9° and 60.9°, indicating the presence of laponite. As shown in Fig. S2(b), the laponite exhibited four diffraction peaks at 6.98°, 19.7°, 34.9°, and 61.32°, corresponding to the (001), (100), (105), and (300) crystal planes (Lyu et al., 2024). Interestingly, the (001) diffraction peak completely disappeared in SPG-L and SPG-B, demonstrating the exfoliation and uniform dispersion of laponite in SPG-L and SPG-B. The exfoliation and uniform dispersion of laponite are critical for maximizing its reinforcing capabilities. Exfoliation ensures that individual laponite platelets, with their high surface area and aspect ratio, are fully separated, enabling effective interaction with the surrounding matrix. Uniform dispersion prevents agglomeration, ensuring that the reinforcement is evenly distributed throughout the material.

XPS spectrum provides additional evidence regarding the surface chemistry and elemental makeup of polymer (Figs. 1(d) and S3–S6) (Ye et al., 2024). The result indicated the existence of C, N, O, and S in all samples, with new peaks of Si and Li detected after the addition of laponite. Particularly, high-resolution C 1*s* peak of the SPG-N was decomposed into three peaks at binding energies of 288.0, 286.1, and 284.8 eV. High-resolution N 1*s* peak of

the SPG-N was decomposed into two peaks at binding energies of 400.4 and 399.6 eV, corresponding to the –N–H– and C–$NH_2$ functional groups, respectively. Upon incorporating CNFs, the peaks associated with C=O/–O–C–O–, C–N/C–O, –N–H, and C–$NH_2$ functional groups shifted to binding energies of 288.2, 285.7, 400.3, and 399.3 eV, respectively, further confirming the role of CNFs in enhancing H-bonding within SPG-N. Following the incorporation of laponite, peaks corresponding to C=O/–O–C–O–, C–N/C–O, –N–H, C–$NH_2$, and Si–O appeared at 288.3, 286.0, 400.1, 399.4, and 102.2 eV, respectively, via H-bonding and electrostatic interactions. This finding is consistent with previous reports, which indicates that the addition of laponite promoted intermolecular hydrogen and ionic bonding interactions, resulting in shifts in binding energy (Golafshan et al., 2017; Lyu et al., 2024). After incorporating both CNFs and laponite, the above peaks in SPG-B further transitioned to 288.1, 285.5, 400.3, 399.3, and 102.1 eV.

### 3.2. Rheological and adhesive characteristics of SPG-forming suspensions

In examining the potential of SPG as fracture-sealing materials, the rheological properties and interfacial adhesion of the suspension prior to polymer formation are critical for effectiveness in practical applications. Specially, in complex downhole environments, the gel-forming suspension must be pumpable from the wellhead to the reservoir fracture with high shear forces applied and effectively retained within the fracture under low shear conditions. Therefore, an ideal lost circulation solution should possess excellent shear-thinning and thixotropic properties, along with robust adhesion to the rock surfaces of the wellbore.

The variations of suspension viscosity and shear stress with shear rate for different reinforcing materials are shown in Fig. 2(a) and (b), respectively. The suspensions demonstrated shear-thinning behavior with an increase in shear rate (Fig. 2(a)). For example, at shear rates of 0.1 and 100 $s^{-1}$, the viscosities of SPG-N measured 32 and 5 mPa·s, respectively. Incorporating CNFs, laponite or both significantly enhanced the viscosity. For example, when both CNFs and laponite were added, the viscosity at 0.1 $s^{-1}$ rose to 2268 mPa·s. This indicates that laponite together with high-aspect-ratio CNFs, through hydrogen bonding and electrostatic interactions, formed an effective network within the polymer matrix, thereby increasing viscosity at low shear rates, i.e., a key property for preventing lost circulation in reservoir fractures. Similarly, the addition of CNFs and laponite increased shear stress (Fig. 2(b)). The power-law and Herschel–Bulkley models were employed to fit the experimental shear stress–shear rate curves, with high regression coefficients ($R^2 > 0.99$) (Tables S2 and S3), confirming their accuracy in describing the rheological behavior of the suspensions. Analyzing of the flow behavior index ($n$) and the consistency coefficient ($K$) revealed that SPG-B exhibited the lowest $n$ while the highest $K$, suggesting that the combined use of CNFs and laponite favored shear thinning behavior in the gel-forming suspensions. Shear-thinning behavior is advantageous as it enhances pumpability and retention, i.e., low viscosity facilitates flow under shear, while high viscosity ensures retention within fractures. The yield stress ($\tau_0$) is the minimum stress that must be applied to a material to initiate flow. It was observed that $\tau_0$ also increased with CNFs and laponite addition, reflecting the formation of robust structural network that enhances the material's resistance to deformation and improves its stability under low-stress conditions.

Thixotropic properties refer to the ability of gel-forming suspension to exhibit a reversible reduction in viscosity under applied shear stress and regain their initial viscosity upon stress removal. This property is particularly valuable for fracture-sealing suspensions, which require easy flow during shear-induced pumping and structural recovery afterward to ensure stability and effectiveness. To simulate this behavior, the thixotropy was studied using a three-stage test (Fig. 2(c)). Particularly, the three-stage experiment examined viscosity changes at three shear rates of $10^{-2}$, $10^{1}$, and back to $10^{-2}$ $s^{-1}$. It was observed that as the shear rate increased from $10^{-2}$ to $10^{1}$ $s^{-1}$, SPG-N exhibited minimal change in the viscosity. However, the addition of CNFs, laponite, or both significantly enhanced the change in the viscosity due to the enhanced shear-thinning effect. When the shear rate decreased back to $10^{-2}$ $s^{-1}$, the viscosity of all samples recovered. Notably, SPG-B recovered more rapidly than SPG-C and SPG-L, demonstrating the superior thixotropic properties (Huang et al., 2022a).

The unique flow behavior of SPG-B is schematically illustrated in Fig. 2(g). At rest, the presence of hydrogen bonds and electrostatic interactions within the gel-forming suspension ensured the robust network, resulting in high viscosity (Fig. 2(g1)). Upon shearing, the network of gel-forming suspension was disrupted, leading to the decrease in viscosity (Fig. 2(g2)). As the shear rate increased further, the alignment of both CNFs and laponite in the direction of flow occured, resulting in a significant reduction in viscosity (Fig. 2(g3)) (Corzo et al., 2023; Mancilla et al., 2024). This behavior is known as shear-thinning. However, when the shearing ceased, the hydrogen bonds and electrostatic interactions drove the rebuilding of the robust network, leading to a rapid recovery in robust network and viscosity (Fig. 2(g1)), i.e., thixotropic properties (Angelini et al., 2014; Dávila and d'Ávila, 2019).

The adhesion of gel-forming suspensions to fracture walls is another critical factor in ensuring their effective retention within the reservoir fractures. Strong adhesion enables the suspension to firmly anchor to the rock surfaces, reducing the risk of displacement by formation fluids or high-pressure conditions. This property is essential for maintaining a stable barrier within the fracture, thereby enhancing the overall sealing efficiency and longevity of the suspension in downhole applications. Enhanced adhesion also contributes to the formation of a robust and cohesive network that optimizes the interaction between the formed gels and the fracture walls, further improving its sealing and fluid-blocking capabilities. Herein, quartz plate served as mould for evaluating the adhesive properties of suspensions via interfacial tension instrument (Figs. 2(d), (e), and S7).

The test process consisted of five phases, i.e., approach, contact, retraction, detachment, and return. The maximum adhesive force ($D$) was recorded between the retraction and detachment process, representing the maximum degree of adhesion between the suspensions and the quartzite core slices. For SPG-N gel-forming suspension, the maximum adhesive force was only 0.010 mN (Fig. 2(d)). The addition of CNFs, laponite, and a combination of both increased the maximum adhensive force to 0.036, 0.056, and 0.072 mN, respectively (Figs. 2(e) and (f), and S7). CNFs and laponite possess nanoscale dimensions and abundant hydroxyl groups. These properties increase the contact surface area and create supplementary bonding sites, leading to strong adhesion that ensures the effective retention within the reservoir fractures.

### 3.3. Transport and filling characteristics of suspensions within fractures

To gain deeper insights into the potential of suspensions for sealing applications in complex geological environments, further investigations on the transport and filling behavior were conducted. Two different visualized fracture models, i.e., wedge-shaped and parallel fractures with varying degrees of inclination (0°, 45°, and 90°) were employed (Figs. 3 and S8). This approach was designed to provide an intuitive comprehension of the transport pathways and

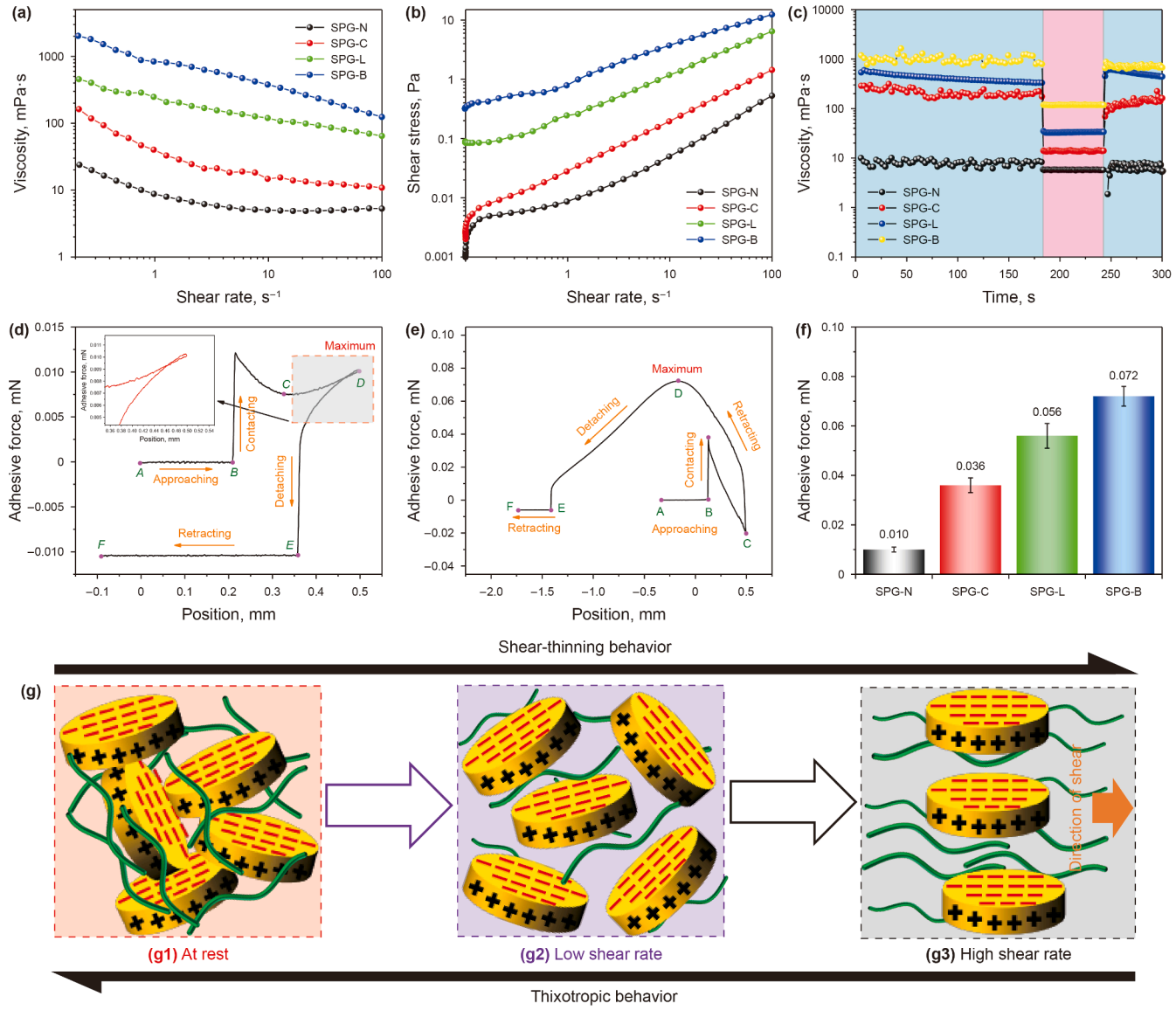


**Fig. 2.** Rheological and adhesive behavior of gel-forming suspensions: (**a**) steady-state viscosity versus shear rate, (**b**) shear stress versus shear rate, (**c**) thixotropic behavior, (**d**) adhesive force of SPG-N, (**e**) adhesive force of SPG-B, (**f**) adhesive forces of SPGs with different reinforcing materials, and (**g**) schematic of the gel-forming suspension at rest, under a low shear rate, and under a high shear rate.

filling efficiency of the suspensions within simulated fractures. The tests offered a visual representation of suspension behavior within fractures, laying the groundwork for optimizing its application in downhole to seal formation fractures effectively.

The transport and filling behavior of suspensions in a wedge-shaped fracture are presented in Figs. 3(b) and S9. Observations indicated that the inclusion of CNFs and laponite facilitated efficient sealing around the wellbore. Specially, the SPG-N gel-forming suspensions showed a greater tendency to fill the lower portion of the fracture, with inclination angles (IA) consistently below 30° in all instances (Figs. 3(b), (c), and S9). However, upon incorporating CNFs and laponite, the suspensions exhibited higher IA during transport (e.g., 49.24° at 1 min, 49.72° at 3 min, 50.89° at 5 min, and 57.51° at 7 min). Additionally, at 7 min, the filling degree (FD) of SPG-B gel-forming suspension was 30% higher than that of SPG-N gel-forming suspension (Fig. 3(c)).

Considering the complexity of stratum fractures, the transport and filling behavior of SPG-B suspension were further examined in parallel fractures with specific inclination angles (i.e., 0°, 45°, and 90°) (Fig. 3(d)–(i)). When the fracture inclination angle was 0°, gravity acted perpendicular to the fracture plane. In this scenario, gravity did not contribute as a driving force, and the suspension was primarily driven by its own mobility and the pressure difference within the fracture. It was observed that the inclination angles of the SPG-B suspension at various injection stages surpassed 90° (Fig. 3(d) and (e)), effectively filling the fractures at an inclination angle of 0°. At a fracture inclination angle of 45°, gravity aligned with the fracture inclination, encouraging a downward flow of the suspension along the fracture. Nevertheless, the strong hydrogen bonding and electrostatic attractions in the SPG-B gel-forming suspension enabled superior suspension stability, resulting in trapezoidal diffusion. The angle between the suspension and the formation still exceeded 60° (Fig. 3(f) and (g)). In fractures with an extreme 90° inclination, gravity acted parallel to the fracture, creating a strong tendency for the suspension to flow downward. However, the inclusion of CNFs and laponite still imparted

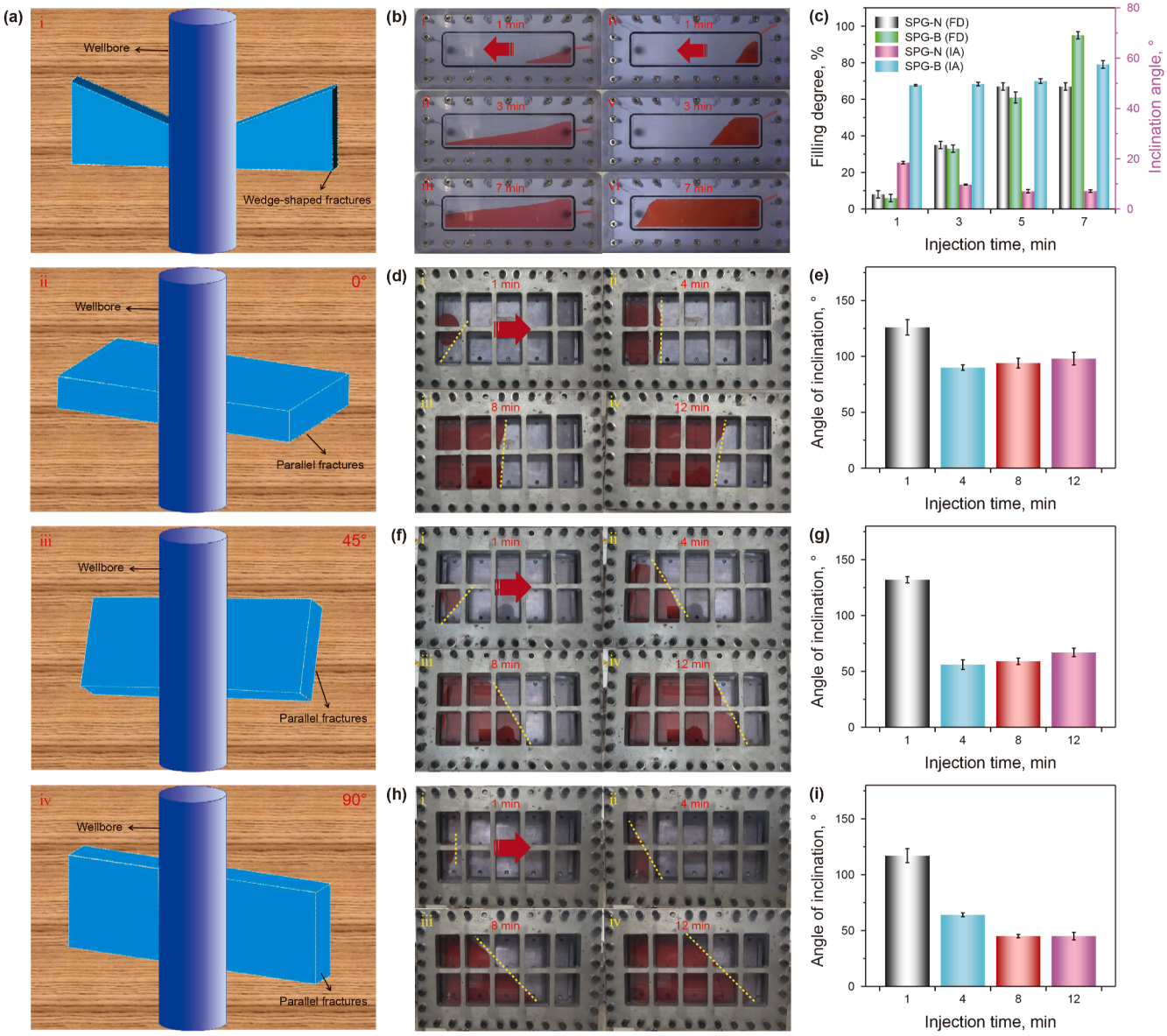


**Fig. 3.** Transport and filling behavior of gel-forming suspensions: (**a**) schematic of fractures with different inclination angles, (**b**) SPG-N (left) and SPG-B (right) at different injection times in a wedge-shaped fracture, (**c**) fracture filling degree (FD) and inclination angle (IA) of the wedge fracture by the suspensions at different injection times, (**d**, **f**, **h**) SPG-B at different injection times in parallel fractures with inclination angles of 0°, 45°, and 90°, respectively, and (**e**, **g**, **i**) IA values of SPG-B suspensions at different injection times in parallel fractures with inclination angles of 0°, 45°, and 90°, respectively.

sufficient retention properties to drastically reduce gravity-induced downflow, thereby enhancing filling efficiency (Fig. 3(h) and (i)). Experimental results confirmed that the SPG-B gel-forming suspension effectively resisted gravitational forces in fractures with varying inclinations, forming stable transport pathways and achieving efficient filling to match different complex geological environments.

### 3.4. Microstructural architecture of SPGs

The excellence in transport and filling properties of suspension ensure their efficient sealing application in complex geological environments. Subsequently, the suspension was polymerized to generate gels, after which their microscopic morphology was examined (Fig. 4(a)–(d)). SPG-N exhibited typically pore structures distributed throughout the gel, characterized by large pore sizes and uneven size distribution (Fig. 4(a)). This phenomenon is likely attributed to the weak interaction between PVA and the monomer. Upon the addition of CNFs, the SPG underwent significant morphological changes specifically, the pore size decreased substantially and the size distribution became homogeneous (Fig. 4(b)). This is attributed to the numerous hydrogen bonds formed between molecules. These strong interactions tightened the molecular network, resulting in smaller pores and a more compact microstructure, which are expected to enhance the mechanical characteristics of the gels (Jin et al., 2022; Shen et al., 2024). Similarly, the incorporation of laponite significantly increased the number of pores while dramatically decreasing pore size (Fig. 4(c)), a finding consistent with observations by Dong et al. (2021). Interestingly, when both CNFs and laponite were added simultaneously to the SPG, the surface of SPG-B became smooth and flat (Fig. 4(d)). This is because laponite and CNFs acted

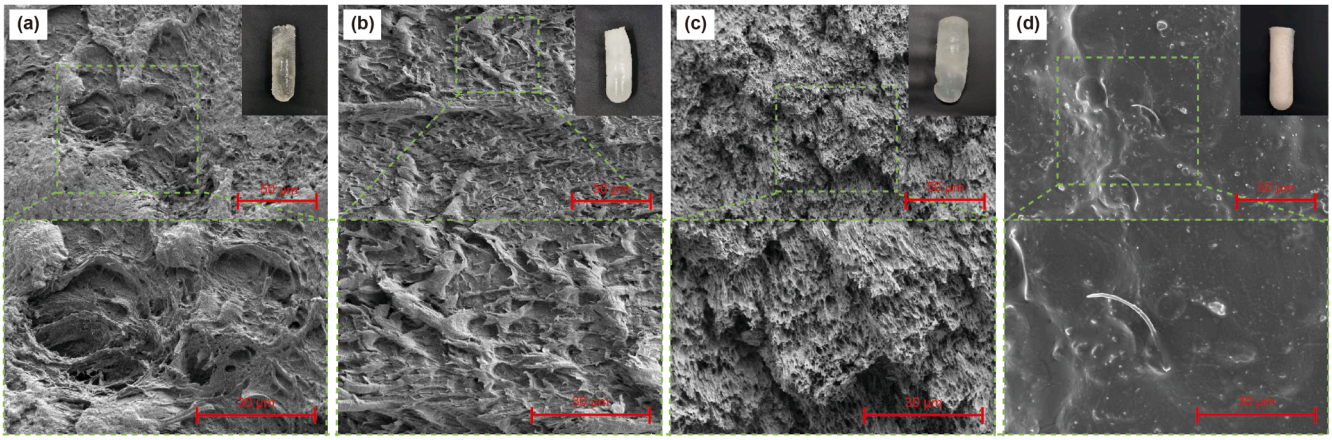


**Fig. 4.** SEM images of synthesized SPGs: (**a**) SPG-N, (**b**) SPG-C, (**c**) SPG-L, and (**d**) SPG-B.

as cross-linking agents, not only providing abundant cross-linking points for the molecular chains but also maintaining the stability of the polymer system through hydrogen bonding and electrostatic interactions, resulting in the formation of a compact film after dying.

### 3.5. Viscoelastic properties of SPGs

To assess the viscoelastic characteristics of SPG, dynamic oscillatory scans were conducted. Particularly, the storage modulus ($G'$) and loss modulus ($G''$) of all samples were measured under constant conditions of 10% strain, respectively (Fig. 5(a)). The $G'$ represents the material's ability to store and recover elastic energy, while the $G''$ quantifies the irreversible energy dissipated by the material in the form of heat. With the addition of CNFs and laponite individually, the storage modulus of the gels showed an upward trend. This is due to both CNFs and laponite enhancing the network structure density of the gels through hydrogen bonding and electrostatic interactions. When CNFs and laponite were added simultaneously, the storage modulus of the SPG increased significantly. For instance, when the strain was fixed at 10%, the $G'$ of SPG-B was 36428 Pa, which was higher than those of SPG-N (8313 Pa), SPG-C (19273 Pa), and SPG-L (29012 Pa) (Fig. 5(b)). The CNFs functioned as reinforcing fillers in the polymer matrix owing to their nanoscale dimensions and high Young's modulus, while laponite contributed additional physical cross-linking points through its nanoscale dimensions and abundant surface charges. Moreover, the negatively charged groups (i.e., $–COO^-$) in CNFs and positively charged groups (i.e., $Mg–OH_2^+$) on the edge surface of laponite formed strong ionic bonding (Šebenik et al., 2020). Therefore, these synergistic reinforcing effects constructed a multi-network structure within the SPG-B, leading to superior viscoelastic properties.

During reservoir application, SPGs are typically subjected to shearing forces, which may damage the gel structure and influence the bearing strength. To evaluate this, the thixotropic properties of SPGs containing different reinforcing materials were assessed through oscillatory deformation at varying strains (Fig. 5(c)). Similarly, with CNFs and laponite acting individually or synergistically, the storage modulus of SPG increased, as observed from the recovery cycling tests. The combination of high strength and nanofibrillated structure of CNFs allowed SPG-C to maintain high stability throughout the oscillatory deformation. On the other hand, laponite interacted with molecular segments through its nanolayered structure and surface activity, resulting in high stability of SPG-L, as well. When both CNFs and laponite were introduced simultaneously, the $G'$ remained unaltered upon altering the strain from 10% to 200% and back to 10% for several cycles. This demonstrates that the SPG-B displayed outstanding thixotropic properties and self-healing capabilities, resulting in superior ability to seal reservoir fractures during different pumping conditions.

The time-dependent oscillatory measurements of SPGs were also evaluated (Fig. 5(d)). The $G'$ of the SPG-N exhibited fluctuations as the oscillation time rose to 360 s, indicating a fragile microstructure. After adding CNFs, the $G'$ quickly recovered to its initial state and then remained stable over time. This suggests that the gel maintained the high-strength network state under external force, likely due to the formation of a more robust structure facilitated by the reinforcement effects of CNFs. Upon the addition of laponite, the gels exhibited minimal impact from external forces. When CNFs and laponite were incorporated simultaneously, the SPG-B maintained its structural integrity under external forces, and hence the $G'$ barely changed. This is ascribed to the combined effects of multiple hydrogen bonds and electrostatic interactions involving CNFs and laponite, significantly enhancing the mechanical robustness and structural integrity of the gel.

### 3.6. Mechanical characteristics of SPGs

The superior reinforcement provided by CNFs and laponite was further validated through comprehensive mechanical property evaluations. Fig. 6(a) illustrates the tensile tests performed on SPG using a InstronTester. As depicted in Fig. 6(b) and (c), SPG-N exhibited a tensile strength of 98±18 kPa and an elongation at break of 1045%±140%, respectively. After introducing CNFs, the tensile strength of the SPG-C increased to 442±35 kPa, with an elongation at break of 3212%±203%, These values were 4.5 and 3.1 times greater than those of SPG-N, respectively. Additionally, the Young's modulus also increased after the addition of CNFs (Fig. 6(d)), consistent with previous studies (Ryu and McClements, 2025). This improvement is attributed to the uniform dispersion of CNFs within the gel matrix and their multiple network structure, making the SPG more resistant to deformation under external forces. Similarly, introducing laponite resulted in SPG-L achieving a tensile strength of 464±57 kPa, a 4.7-fold increase compared to SPG-N. This aligns with earlier findings that laponite formed hydrogen and ionic bonds with poly(AM-DVB-AMPS) chains, enhancing the network density and mechanical properties (Boyaci et al., 2016; Chiang et al., 2024). When CNFs and laponite were

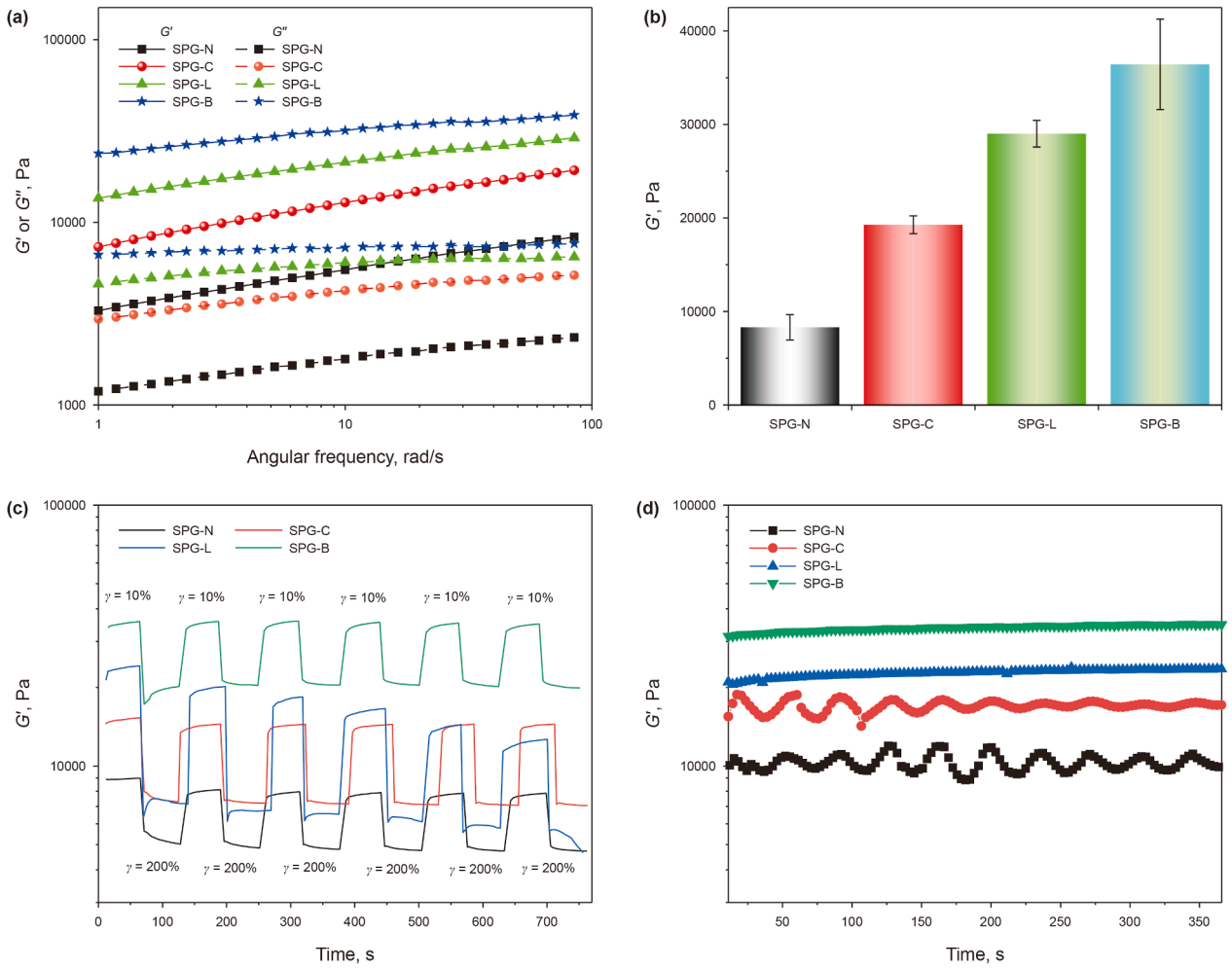


**Fig. 5.** Viscoelastic properties of synthesized SPGs: (**a**) dynamic frequency sweep at a fixed strain of 10%, (**b**) storage modulus ($G'$) at a fixed strain of 10% and an angular frequency of 84 rad/s, (**c**) thixotropic behavior, and (**d**) oscillatory time sweep at a fixed stress of 10 Pa and a frequency of 1 Hz.

added simultaneously, SPG-B exhibited the highest tensile strength and elongation at break values of 735±58 and 3460±330 kPa, respectively.

Cyclic tensile experiments were subsequently conducted to evaluate the fatigue resistance of the SPG (Figs. S10–S12). Polymer gels typically exhibit elastic behavior, with distinct loading/unloading stress–strain curves. Gel toughness refers to the ability of a gel to absorb and dissipate energy without breaking when subjected to external forces such as tension, compression, or deformation. It is a measure of the gel's resistance to fracture and is often quantified as the area under the stress–strain curve obtained from mechanical testing. For SPG-N, subjected to 5 cycles of 500% fixed strain (Figs. S10, S13(a) and (b)), the maximum toughness and tensile strength were 69.25 kJ/m$^3$ and 22.95 kPa, respectively. Upon adding CNFs, the maximum toughness and tensile strength of SPG-C increased to 332.63 kJ/m$^3$ and 103 kPa, representing 4.80- and 4.49-fold enhancements over SPG-N. This enhancement is ascribed to hydrogen-bond interaction, facilitating effective energy absorption and dissipation, thus preserving mechanical properties through multiple cycles. Similarly, laponite improved the maximum toughness and tensile strength to 371.62 kJ/m$^3$ and 115 kPa, representing 5.36- and 5.01-fold increases compared to SPG-N. When CNFs and laponite were combined, the maximum toughness and tensile strength of SPG-B reached as high as 314.62 kJ/m$^3$ and 138 kPa due to their synergistic reinforcing effect.

The cyclic tensile loading and unloading curves of the SPG under different strain levels are presented in Fig. S11. SPG-N had a maximum tensile strength of 22.4 kPa at a strain of 500%. With the simultaneous addition of CNFs and laponite, the roughness and recyclability of the SPG were significantly enhanced at different strain levels ranging from 100% to 500%. At a strain of 500%, the maximum toughness of SPG-B was 163.78 kPa. These results indicate a 7.31-fold increase over SPG-N, demonstrating stable and continuous network integrity during cyclic loading.

Subsequently, we evaluated the recovery performance of the SPG (Figs. S12, S13(c) and (d)). After 1–5 loading/unloading cycles, the energy dissipation values of SPG-N were 10.97, 7.42, 7.69, 7.78, and 7.83 kJ/m$^3$, with the recovery rates of 35%, 36%, 35%, and 35%, respectively. Whereas, for SPG-B, incorporating CNFs and laponite, the energy dissipation values were 69.5, 46.3, 43.7, 43.1, and 43.1 kJ/m$^3$, with the recovery rates of 33%, 37%, 38%, and 38%, respectively. It can be seen that the recovery rate of SPG-N gradually decreased with cycle number, while SPG-B showed a gradual increase in recovery rate with cycle number due to the presence of hydrogen bonding and electrostatic interactions between CNFs, laponite, and the polymer matrix.

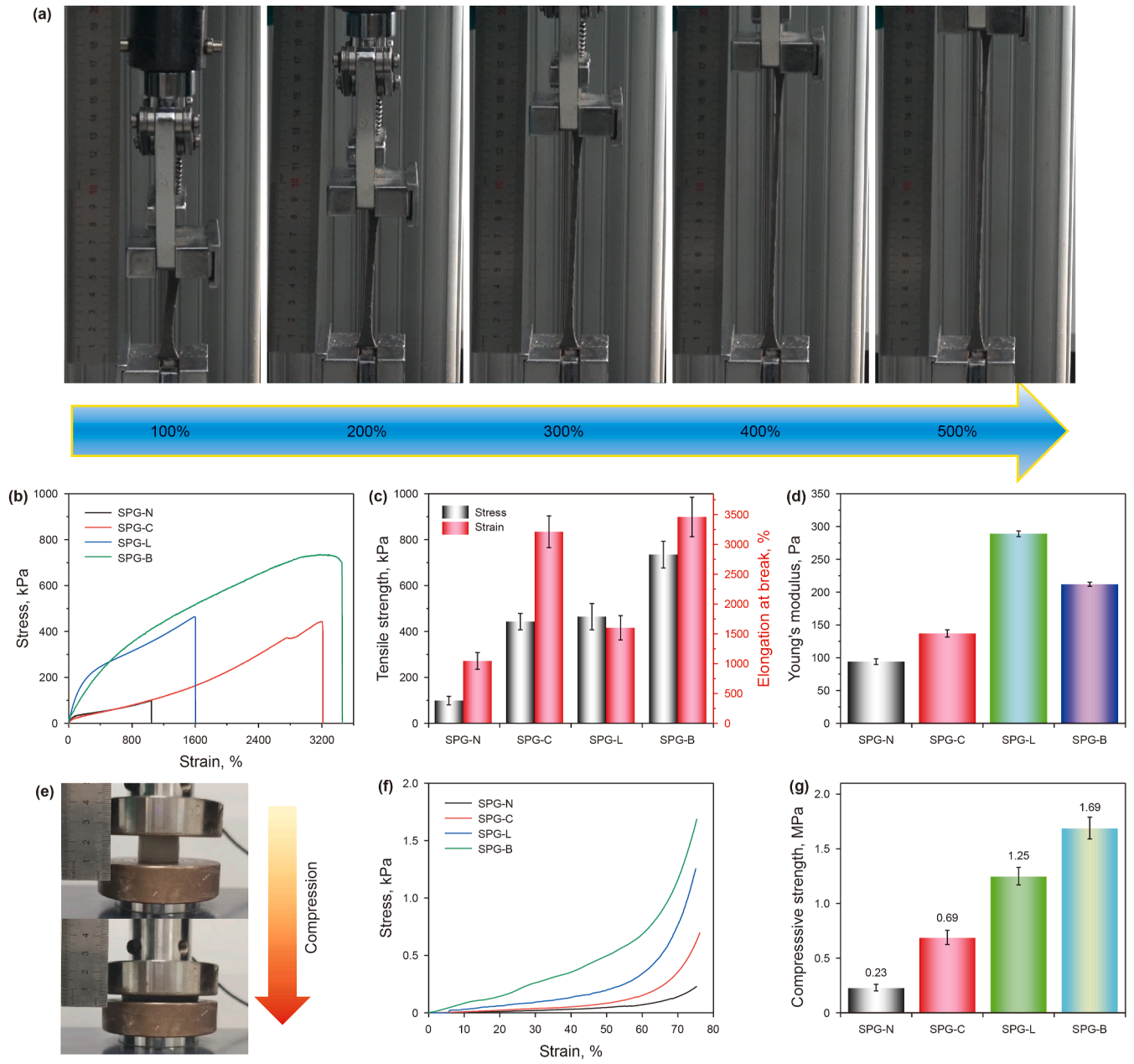


**Fig. 6.** Mechanical properties of synthesized SPGs: (**a**) tensile deformation process under different strain levels, (**b**) typical stress–strain curves, (**c**) tensile strength and elongation at break, (**d**) Young's modulus, (**e**) compressive deformation behavior, (**f**) typical compressive stress–strain curves, and (**g**) compressive strength at a fixed strain of 75%.

Finally, compressive strength tests at 75% strain revealed that CNFs and laponite significantly enhanced the compressive properties of gels (Fig. 6(e)–(g)). The compressive strength of SPG-N, SPG-C, and SPG-L reached 0.23, 0.69, and 1.25 MPa, respectively. Analogous findings were reported by Wu et al. (2024), who observed that CNFs created 3D network skeleton within the polymer matrix, leading to superior compressive strength. Similarly, laponite improved compressive strength through hydrogen bonding and electrostatic interactions, this was in agreement with the findings documented by Jafari et al. (2023). Combining CNFs and laponite in SPG-B resulted in a compressive strength of 1.69 MPa, which is seven times greater than SPG-N, due to the synergistic reinforcement effect. In summary, the combined use of CNFs and laponite significantly enhanced the gel network structure, minimized energy loss, and improved tensile strength, and compressive strength. These enhancements are critical for ensuring the long-term stability and reliable performance of SPG in practical applications.

### 3.7. Sealing characteristics of SPGs

The pressure-bearing and sealing effect of SPG on porous media was evaluated (Fig. 7(a)). This performance reflects the overall ability of material to withstand pressure and effectively block fluid flow within fractures or porous formations. The SPG was in-situ synthesized in the fractured core, followed by a series of sealing tests to determine its maximum pressure-bearing capacity. This was assessed by injecting deionized water at varying flow rates (e.g., 1.99, 3.99, 5.99, 7.99, and 9.99 mL/min) into the sand-filled tubes after the gel had formed (Figs. S14–S17).

As depicted in Fig. 7(b), SPG-B achieved maximum pressure values of 16.94, 16.56, 16.45, 16.09, and 16.01 MPa for flow rates of 1.99–9.99 mL/min, respectively. Although the highest pressure slightly decreased with increasing flow rate, all values exceeded 16 MPa. In contrast, SPG-N, SPG-C, and SPG-L exhibited maximum pressures of 7.37, 12.16, and 13.66 MPa, respectively, at a flow rate of 1.99 mL/min (Fig. 7(b)). At the same flow rate, the combined use of CNFs and laponite led to increases in maximum pressure over 16 MPa, surpassing the previously reported values for polymer gels reinforced with either cellulose or laponite alone (Table S4). For instance, Jiang et al. (2024) reported a cross-linked gel primarily composed of β-cyclodextrin and carboxymethyl cellulose. In water flooding experiments, this gel achieved a maximum pressure of 8.5 MPa in sand-filled pipes with varying permeability. Jia et al. (2020) described a composite gel prepared with sulfonated polyacrylamide, polyethyleneimine, and laponite, which achieved a

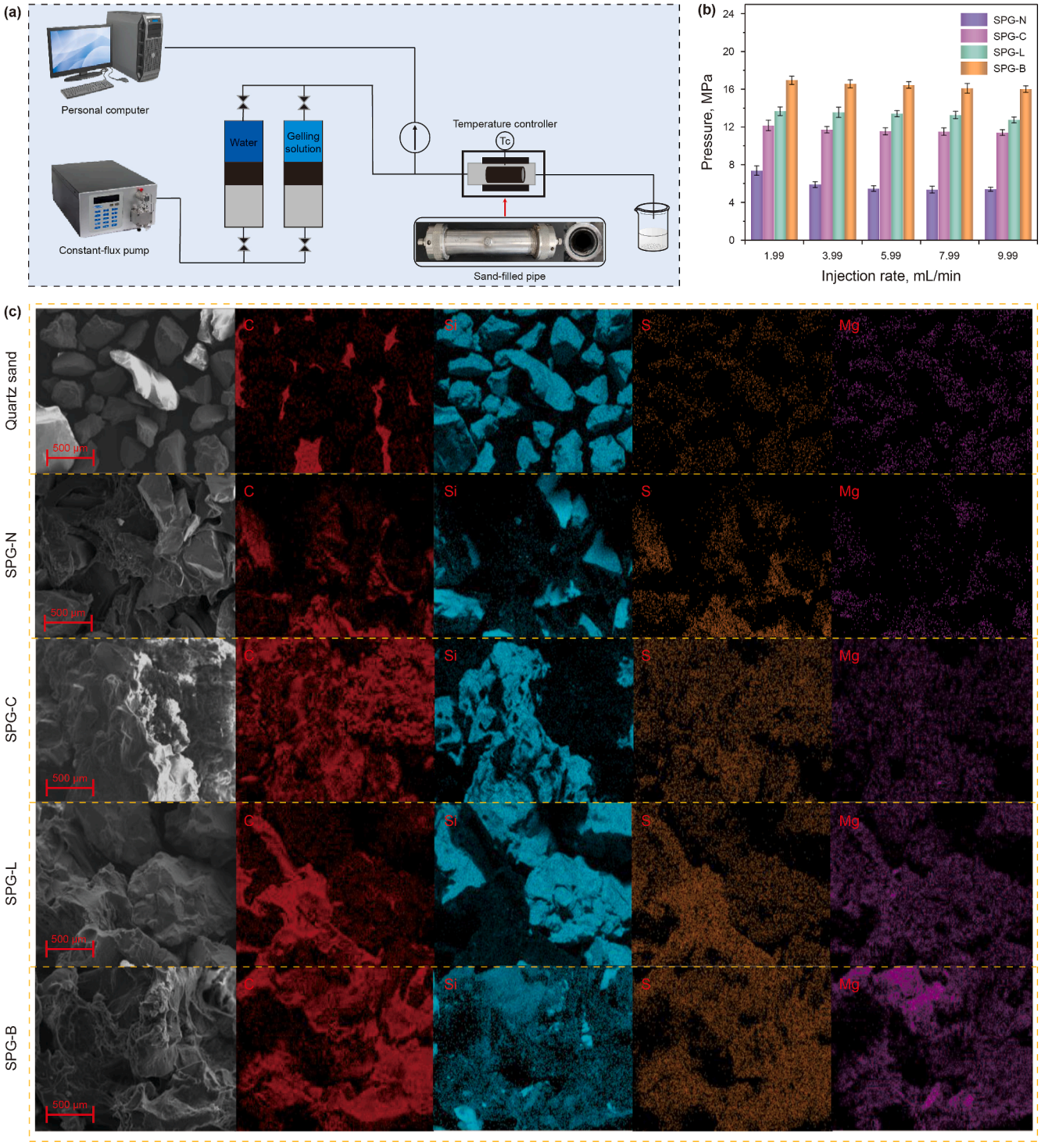


**Fig. 7.** Sealing performance of synthesized SPGs: (**a**) displacement experiment setup, (**b**) maximum breakthrough pressure as a function of injection rate, (**c**) SEM images and EDS elemental maps after filling with SPG-N, SPG-C, SPG-L, and SPG-B.

sealing strength of 1.75 MPa in 0.8 mm fractures using nitrogen gas drive. Despite differences in experimental conditions (e.g., displacement phase type, displacement rate, and fracture size), the significantly higher breakthrough pressure achieved by SPG-B demonstrates its superior and stable pressure-bearing capacity in fracture plugging (Table S4). The presence of double bonds, hydrogen bonds, and electrostatic interactions, along with the reinforcing effects of laponite and CNFs, enhances its ability to withstand pressure and effectively seal fractures.

The superior viscoelastic and mechanical characteristics of SPG are responsible for the high pressure-bearing capacity. In addition, their high adhesion to quartz sand significantly contributes to their pressure-bearing capacity. To explore the mechanism of action of SPG on porous media, we focused on analyzing the microscopic morphological differences of quartz sand before and after gel filling. As depicted in Fig. 7(c), the quartz sand exhibited a relatively loose structure with numerous pores when unfilled. The primary component of the sand (i.e., $SiO_2$), resulted in a high proportion of Si elements. After filling the quartz sand with SPG-C, the internal structure became denser and more compact. Notably, a fibrillated structure was observed, likely due to the presence of CNFs (Fig. S18(b)). Similarly, when the SPG-L was used, a compact internal structure was also observed (Fig. S18(c)). SPG-L predominantly adsorbed onto the surface of quartz sand via hydrogen bonding and electrostatic interactions due to the presence of laponite, as evidenced by significant increases in the Si and Mg elements on the surface of quartz sand (Chen et al., 2022; Ochoa-Cornejo et al., 2016; Qi et al., 1996). When both CNFs and laponite were incorporated into the gel, the pores between the quartz sand grains were effectively coated with the gel (Fig. S18(d)). This synergistic effect ensured optimal adsorption of the gel onto the quartz sand surface, resulting in the strongest adhesion. These findings confirmed the significant contribution of CNFs and laponite to the adhesion properties and pressure-bearing capacity of SPG.

### 3.8. Long-term stability performance of SPGs

Due to the high temperature and high salinity typically encountered in the formation, the application of SPGs for sealing reservoir fractures poses a significant challenge. These extreme conditions can accelerate thermal degradation, weaken bonding interactions, leading to reduced mechanical strength and pressure-bearing capacity over time. To evaluate the effect of salinity and temperature, the SPG-B gels were synthesized in the presence of brine (70,000 mg/L $Na^+$ and 16,000 mg/L $Ca^{2+}$, targeted for the Tahe heavy oil block, Table S5). The as-prepared SPG-B gels were then aged using a hot-rolling oven over different aging periods (i.e., 0, 5, 10, 15, 20, and 30 d) at 120 °C. The chosen salinity and temperature matched the targeted formation conditions.

It was observed that the gel color gradually became dark as the aging time proceed (Figs. 8(a) and (b), and S19). The progressive darkening of the gel with time was primarily attributed to incomplete oxidation and thermal decomposition of the SPG matrix. To quantify the degradation, the modulus of the SPG was further tested (Figs. S20 and S21). It was observed that at an angular frequency of 84 rad/s, the storage modulus of SPG-B synthesized without adding brine declined from 31362 to 15653 Pa over 30 d of aging. (Figs. 8(c) and S20), reflecting a 50% reduction in storage modulus. Furthermore, SPG-B synthesized in the presence of brine also exhibited strength loss during high-temperature aging, with a 45% reduction in storage modulus after aging for 30 d (Figs. 8(d) and S21). Furthermore, the presence of salt reduced the storage modulus of SPG-B (Fig. 8(e)) attributed to the electrostatic shielding effect exhibited by $Na^+$ and $Ca^{2+}$ in gel-forming suspensions, where the disruption of hydrogen bonding and electrostatic interactions resulted in a reduction in gel strength (Grossmann et al., 2023; Lei et al., 2025). Despite the presence of salt and aging treatments impaired the structure integrity of SPG-B, the SPG-B still gelled and exhibited a favorite storage modulus of 6820 Pa after aging for 30 d, ensuring their long-term fracture-sealing application in deep formation.

### 3.9. Degradability of SPGs

In oil and gas well operations, effective removal of gel after sealing is crucial for maintaining productivity, as residual material can clog the formation and reduce hydrocarbon extraction. Therefore, biodegradability has become a key consideration for supramolecular gels. In the present study, we investigated the effects of hydrochloric acid concentration, temperature, and degradation time on the degradation performance of SPG-B. Samples were placed in heat-resistant bottles and sealed. Experiments were conducted to study the degradation of the gels in hydrochloric acid solutions at temperatures of 80–120 °C, using acid concentrations of 5%, 10%, and 15% (Figs. 9 and S22).

The experimental data demonstrate a continuous increase in the degree of gel degradation with time. Taking an environment of 100 °C and 10% HCl as an example, the degradation degree of the gel gradually increased from 7% to 72% within 6–168 h, with 72 h being a critical turning point, where the degradation degree increased sevenfold compared to the initial stage, indicating that the gel network began to significantly decompose.

Hydrochloric acid concentration has a significant effect on gel degradation. At 100 °C, after 72 h, the degradation rates of gels in 5%, 10%, and 15% HCl environments reached 37%, 51%, and 61%, respectively, confirming that high-concentration acid environments can more efficiently disrupt the internal structure of gels and accelerate the degradation process. At the same time, temperature is also an important factor affecting degradation. Under 15% HCl conditions, after 168 h, the degradation degrees at 80, 100, and 120 °C were 62%, 80%, and 96%, respectively. This phenomenon can be attributed to the formation mechanism of SPG, based on hydrogen bonding between CNF, laponite, PVA and cross-linked polymers, whose bond energy is relatively low (20–40 kJ/mol) and easily dissociates in acidic and high-temperature environments (Chen et al., 2023; Hu et al., 2021). The findings of this study demonstrate that the degradation degree of SPG can be precisely controlled by regulating hydrochloric acid concentration, temperature, and time. The results obtained provide a reference for controlling gel stability and degradation curves in practical applications and offer important theoretical support for different drilling conditions.

## 4. Conclusions

This research reports the synthesis of SPG incorporating covalent bonds, crosslinking structure, multiple hydrogen bonding, and electrostatic interactions. Particularly, the SPG was successfully synthesized using a one-pot free radical polymerization method with AM, AMPS, and DVB as the primary covalent monomers, PVA as non-covalent component, and CNFs and laponite as reinforcing fillers. The suspension demonstrated excellent pseudoplastic behavior, thixotropy, and adhesion performance, ascribed to the establishment of multiple hydrogen and ionic interactions, leading to superior filling and retention performance in different shapes of fracture with varying inclination degrees. After the gelling, the SPG reinforced by CNFs and laponite exhibited high tensile strength of 735±58 kPa, elongation at 3460±330 kPa, Young's modulus at 212±3.15 Pa, and compressive strength at 1.69 MPa, as well as a

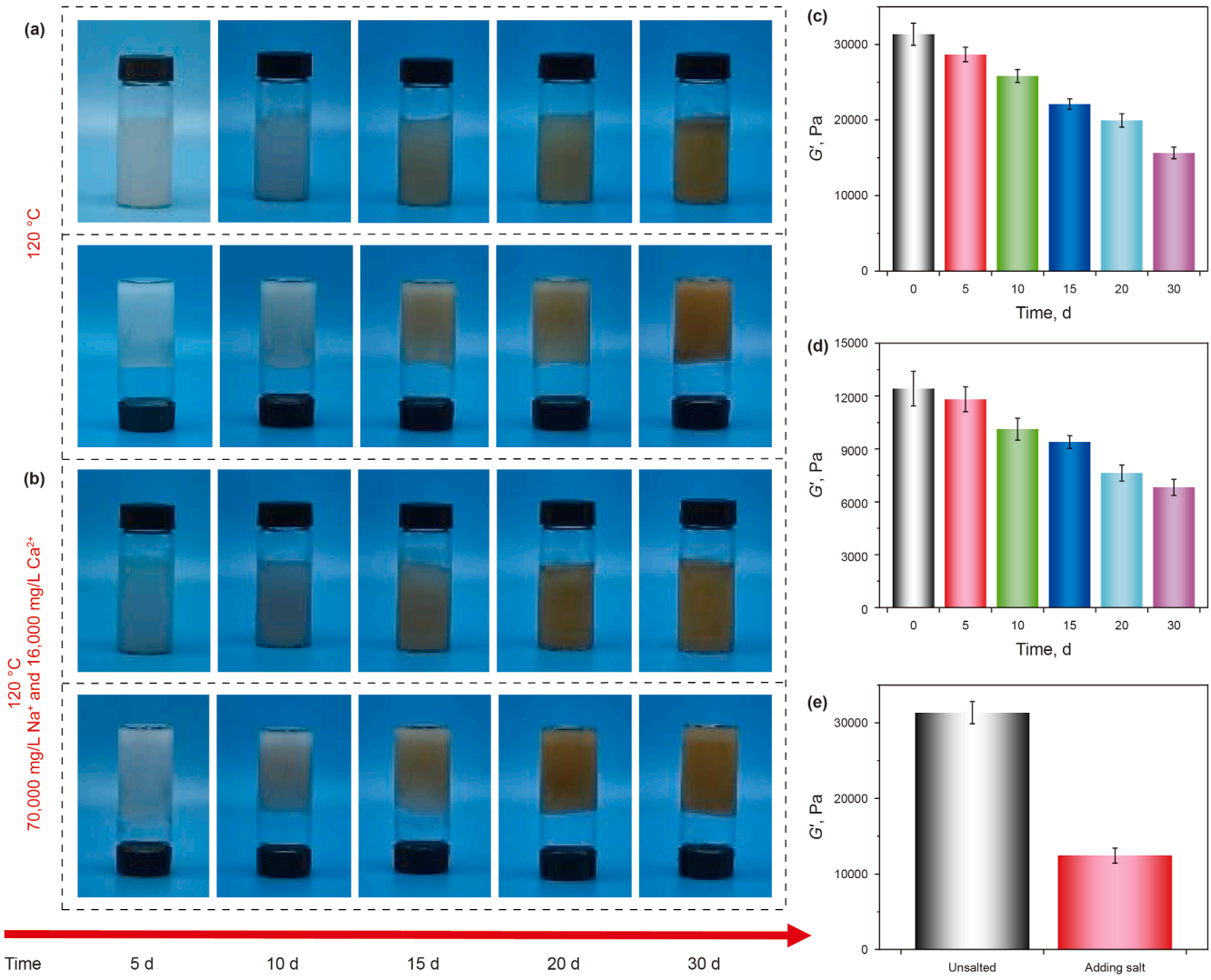


**Fig. 8.** Long-term stability of the synthesized SPGs: (**a**) macroscopic states of SPG-B at different aging times, (**b**) macroscopic states of SPG-N with brine at different aging times, (**c**) $G'$ of SPG-N after aging at different stages, (**d**) $G'$ of SPG-N with brine after aging at different stages, and (**e**) $G'$ of gels formed with and without brine before aging.

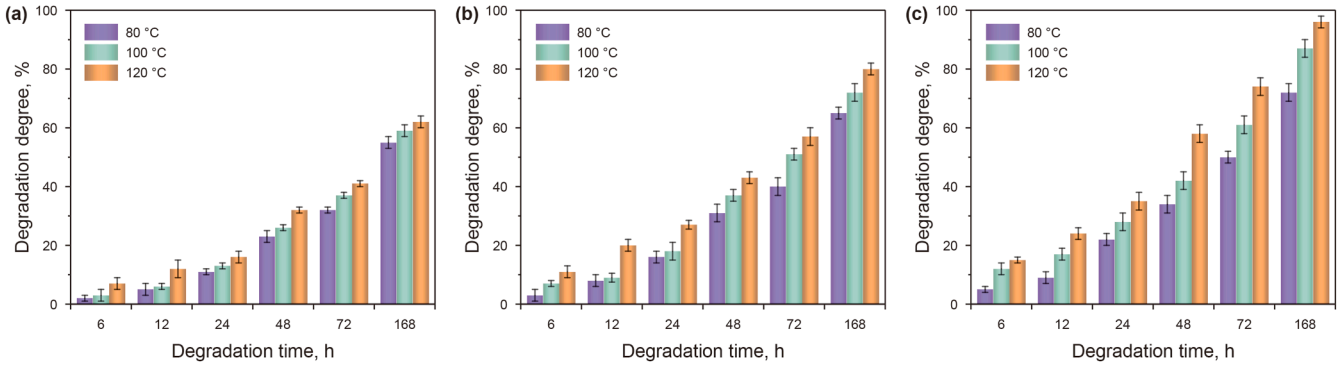


**Fig. 9.** Degradation properties of synthesized SPGs under different HCl concentrations: (**a**) 5%, (**b**) 10%, and (**c**) 1%.

high pressure-bearing capacity of over 16 MPa in porous media. The superior viscoelastic and mechanical properties of SPG, as well as their strong adhesion to quartz sand are responsible for the high pressure-bearing capacity. Moreover, after brine contamination and 30 d of hot aging, the SPG still exhibited a high strength, demonstrating their potential for long-term fracture-sealing applications in deep formations.

The results of laboratory testing provide compelling evidence for the feasibility and efficacy of SPGs in oilfield applications. The one-pot synthesis process employed for this gel system

significantly streamlines preparation, effectively reducing production costs compared to multi-step methods. More importantly, SPGs exhibit outstanding mechanical properties, long-term stability, and resistance to contamination. This substantially decreases the need for frequent well interventions due to repeated sealing procedures, thereby lowering overall operational costs. Preliminary economic assessments indicate that the cost of SPG-B formulation materials is approximately \$972.3/$m^3$ (Table S6), demonstrating favorable potential for industrial application. To enhance industrial applicability, future work will focus on optimizing raw material costs (e.g., replacing CNFs with more cost-effective alternatives) and scaling up the one-pot synthesis process for field deployment. Key challenges include balancing mechanical performance with economic efficiency and developing in-situ gelation protocols suitable for complex wellbore conditions.

## CRediT authorship contribution statement

**Li-Yao Dai:** Writing – original draft, Investigation, Formal analysis, Data curation. **Jin-Sheng Sun:** Supervision, Project administration. **Kai-He Lv:** Resources, Methodology. **Ying-Rui Bai:** Data curation. **Bo Liao:** Formal analysis. **Dong-Qing Yang:** Investigation. **Chao-Zheng Liu:** Formal analysis. **Mei-Chun Li:** Writing – review & editing, Supervision, Project administration, Conceptualization.

## Declaration of competing interest

The authors declare that they have no known competing financial interests or personal relationships that could have appeared to influence the work reported in this paper.

## Acknowledgements

This work was supported from the National Natural Science Foundation of China (52474021, U24B2030), the Natural Science Foundation of Shandong Province (ZR2023ME131), the Basic Science Center Project of the National Natural Science Foundation of China (52288101) “Flow Control of Ultra-deep and Extra-deep Oil and Gas Drilling”, and the Jiangsu Specially-Appointed Professor Program.

## Supplementary data

Supplementary data to this article can be found online at https://doi.org/10.1016/j.petsci.2025.12.037.

## References

Adelnia, H., Ensandoost, R., Shebbrin Moonshi, S., et al., 2022. Freeze/thawed polyvinyl alcohol hydrogels: Present, past and future. Eur. Polym. J. 164, 110974. https://doi.org/10.1016/j.eurpolymj.2021.110974.

Angelini, R., Zaccarelli, E., de Melo Marques, F.A., et al., 2014. Glass–glass transition during aging of a colloidal clay. Nat. Commun. 5 (1), 4049. https://doi.org/10.1038/ncomms5049.

Appel, E.A., del Barrio, J., Loh, X.J., et al., 2012. Supramolecular polymeric hydrogels. Chem. Soc. Rev. 41 (18), 6195–6214. https://doi.org/10.1039/C2CS35264H.

Aslani, F., Zhang, Y., Manning, D., et al., 2022. Additive and alternative materials to cement for well plugging and abandonment: A state-of-the-art review. J. Petrol. Sci. Eng. 215, 110728. https://doi.org/10.1016/j.petrol.2022.110728.

Bai, J., Navara, A.M., Zhao, L., et al., 2022. Harnessing electrostatic interactions for enhanced printability of alginate-based bioinks. Bioprinting 27, e00215. https://doi.org/10.1016/j.bprint.2022.e00215.

Bercea, M., 2024. Recent advances in poly(vinyl alcohol)-based hydrogels. Polymers 16 (14), 2021. https://doi.org/10.3390/polym16142021.

Boyaci, T., Orakdogen, N., 2016. Poly(*N,N*-dimethylaminoethyl methacrylate-co-2-acrylamido-2-methyl-propanosulfonic acid)/laponite nanocomposite hydrogels and cryogels with improved mechanical strength and rapid dynamic properties. Appl. Clay Sci. 121–122, 162–173. https://doi.org/10.1016/j.clay.2015.12.018.

Chen, L., Li, G., Chen, Y., et al., 2022. Thixotropy research of laponite-hydrogel composites for water shutoff in horizontal wells. J. Petrol. Sci. Eng. 208, 109600. https://doi.org/10.1016/j.petrol.2021.109600.

Chen, S., Wang, Y., Yang, L., et al., 2023. Biodegradable elastomers for biomedical applications. Prog. Polym. Sci. 147, 101763. https://doi.org/10.1016/j.progpolymsci.2023.101763.

Chen, Y.-f., Pu, W.-f., Liu, X.-l., et al., 2019. A preliminary feasibility analysis of in situ combustion in a deep fractured-cave carbonate heavy oil reservoir. J. Petrol. Sci. Eng. 174, 446–455. https://doi.org/10.1016/j.petrol.2018.11.054.

Chiang, P.-Y., Zeng, P.-H., Yeh, Y.-C., 2024. Luminescent lanthanide-containing gelatin/polydextran/laponite nanocomposite double-network hydrogels for processing and sensing applications. Int. J. Biol. Macromol. 260, 129359. https://doi.org/10.1016/j.ijbiomac.2024.129359.

Corzo, I.J.M., da, Fonsêca, J.H.L., d'Ávila, M.A., 2023. Influence of carboxymethyl cellulose solutions on rheological properties of laponite dispersions. Rheol. Acta 62 (7), 393–404. https://doi.org/10.1007/s00397-023-01401-3.

Dai, L., Sun, J., Lv, K., et al., 2025a. Influences of reservoir conditions on the performance of cellulose nanofiber/laponite-reinforced supramolecular polymer gel-based lost circulation materials. Gels 11 (7), 472. https://doi.org/10.3390/gels11070472.

Dai, L., Sun, J., Lv, K., et al., 2025b. Cellulose nanofiber-reinforced supramolecular polymer gels for temporary plugging of fractured oil and gas reservoirs. Carbohydr. Polym. 356, 123370. https://doi.org/10.1016/j.carbpol.2025.123370.

Dávila, J.L., d'Ávila, M.A., 2019. Rheological evaluation of laponite/alginate inks for 3D extrusion-based printing. Int. J. Adv. Manuf. Technol. 101 (1), 675–686. https://doi.org/10.1007/s00170-018-2876-y.

de Oliveira, R.L., da Silva Barud, H., De Salvi, D.T.B., et al., 2015. Transparent organic–inorganic nanocomposites membranes based on carboxymethylcellulose and synthetic clay. Ind. Crop. Prod. 69, 415–423. https://doi.org/10.1016/j.indcrop.2015.02.015.

Dong, L., Bu, Z., Xiong, Y., et al., 2021. Facile extrusion 3D printing of gelatine methacrylate/laponite nanocomposite hydrogel with high concentration nanoclay for bone tissue regeneration. Int. J. Biol. Macromol. 188, 72–81. https://doi.org/10.1016/j.ijbiomac.2021.07.199.

Dong, S., Li, L., Wu, Y., et al., 2023. Preparation and study of polyvinyl alcohol gel structures with acrylamide and 2-acrylamido-2-methyl-1-propanesulfonic acid for application in saline oil reservoirs for profile modification. ACS Appl. Mater. Interfaces 15 (11), 14788–14799. https://doi.org/10.1021/acsami.2c22911.

Golafshan, N., Rezahasani, R., Tarkesh, Esfahani M., et al., 2017. Nanohybrid hydrogels of laponite: PVA-Alginate as a potential wound healing material. Carbohydr. Polym. 176, 392–401. https://doi.org/10.1016/j.carbpol.2017.08.070.

Grossmann, L., McClements, D.J., 2023. Current insights into protein solubility: A review of its importance for alternative proteins. Food Hydrocoll. 137, 108416. https://doi.org/10.1016/j.foodhyd.2022.108416.

Gu, S., Wang, H., Wang, Y., et al., 2023. Thermosensitive nanocomposite hydrogel composed of PVPylated poly(D,L-alanine) and laponite as an injectable and bioactive biomaterial. Chem. Eng. J. 466, 143128. https://doi.org/10.1016/j.cej.2023.143128.

Guo, C., Jiang, G., Guan, J., et al., 2024a. Preparation and performance evaluation of a thixotropic polymer gel for loss circulation control. Fuel 371, 132148. https://doi.org/10.1016/j.fuel.2024.132148.

Guo, P., Qiu, Z., Zang, X., et al., 2024b. Epoxy resin microencapsulated by complex coacervation as physical-chemical synergetic lost circulation control material. Energy 293, 130630. https://doi.org/10.1016/j.energy.2024.130630.

Han, Z., Yang, X., Ren, N., et al., 2025. Dynamic sealing mechanisms of drilling fluid in fractured coalbed methane formations: A coupled CFD-DEM numerical study. Comput. Geotech. 188, 107560. https://doi.org/10.1016/j.compgeo.2025.107560.

Hu, D., Zeng, M., Sun, Y., et al., 2021. Cellulose-based hydrogels regulated by supramolecular chemistry. SusMat 1 (2), 266–284. https://doi.org/10.1002/sus2.17.

Huang, F., Lv, J., Li, H., et al., 2022a. Regulation rule of cellulose nanocrystals on thixotropy of hydrogel for water shutoff in horizontal wells. Colloids Surf. A Physicochem. Eng. Asp. 643, 128735. https://doi.org/10.1016/j.colsurfa.2022.128735.

Huang, X., Li, R., Duan, Z., et al., 2022b. Supramolecular polymer gels: From construction methods to functionality. Soft Matter 18 (20), 3828–3844. https://doi.org/10.1039/D2SM00352J.

Jafari, H., Namazi, H., 2023. pH-sensitive biosystem based on laponite RD/chitosan/polyvinyl alcohol hydrogels for controlled delivery of curcumin to breast cancer cells. Colloids Surf. B Biointerfaces 231, 113585. https://doi.org/10.1016/j.colsurfb.2023.113585.

Jia, H., Xie, D.-S., Kang, Z., 2020. Secondary surface modified laponite-based nanocomposite hydrogel for gas shutoff in wellbore. J. Petrol. Sci. Eng. 191, 107116. https://doi.org/10.1016/j.petrol.2020.107116.

Jiang, Z., Yang, H., Ji, Z., et al., 2024. Lignocellulosic hydrogel for profile control and water plugging in high salt reservoirs. J. Mol. Liq. 401, 124707. https://doi.org/10.1016/j.molliq.2024.124707.

Jin, X., Qu, R., Wang, Y., Yong, Wang, et al., 2022. Effect and mechanism of acid-induced soy protein isolate gels as influenced by cellulose nanocrystals and microcrystalline cellulose. Foods 11 (3), 461. https://doi.org/10.3390/foods11030461, 11.

Kang, Y., Ma, C., Xu, C., et al., 2023. Prediction of drilling fluid lost-circulation zone based on deep learning. Energy 276, 127495. https://doi.org/10.1016/j.energy.2023.127495.

Lei, Y., Yue, J., Min, T., et al., 2025. The strengthening effects of different types of salt on the mechanical properties of soy protein isolate and pea protein isolate

composite gels. Food Hydrocoll. 162, 110988. https://doi.org/10.1016/j.foodhyd.2024.110988.
Li, C., Bai, J., Jiang, Y., et al., 2024a2024. Investigating the seepage control and plugging capabilities of polyurethane-cement composites: A comprehensive study on material properties. Constr. Build. Mater. 416, 135191. https://doi.org/10.1016/j.conbuildmat.2024.135191.
Li, J., Wei, P., Xie, Y., et al., 2022. Conjoined-network induced highly tough hydrogels by using copolymer and nano-cellulose for oilfield water plugging. J. Ind. Eng. Chem. 109, 161–172. https://doi.org/10.1016/j.jiec.2022.01.038.
Li, M.-C., Wu, Q., Moon, R.J., et al., 2021. Rheological aspects of cellulose nanomaterials: governing factors and emerging applications. Adv. Mater. 33 (21), 2006052. https://doi.org/10.1002/adma.202006052.
Li, M.-C., Wu, Q., Song, K., et al., 2015. Cellulose nanoparticles: Structure–morphology–rheology relationships. ACS Sustain. Chem. Eng. 3 (5), 821–832. https://doi.org/10.1021/acssuschemeng.5b00144.
Li, Z., Hou, Z., Fan, H., et al., 2017. Organic–inorganic hierarchical self-assembly into robust luminescent supramolecular hydrogel. Adv. Funct. Mater. 27 (2), 1604379. https://doi.org/10.1002/adfm.201604379.
Li, Z., Lin, L., Luo, Y., et al., 2024b. Carboxymethylcellulose–laponite nanocomposites as a temperature-resistant rheological modifier. J. Mater. Sci. 59 (40), 19057–19074. https://doi.org/10.1007/s10853-024-10325-z.
Lin, C., Taleghani, A.D., Kang, Y., et al., 2022. A coupled CFD-DEM simulation of fracture sealing: Effect of lost circulation material, drilling fluid and fracture conditions. Fuel 322, 124212. https://doi.org/10.1016/j.fuel.2022.124212.
Lin, C., Xu, Q.-C., Han, L.-X., et al., 2024. Fracture sealing performance of granular lost circulation materials at elevated temperature: A theoretical and coupled CFD-DEM simulation study. Pet. Sci. 21 (1), 567–581. https://doi.org/10.1016/j.petsci.2023.10.002.
Liu, Y., Jiang, D., Wu, Z., et al., 2024. Highly conductive and sensitive acrylamide-modified carboxymethyl cellulose/polyvinyl alcohol composite hydrogels for flexible sensors. Sensor Actuator Phys. 370, 115258. https://doi.org/10.1016/j.sna.2024.115258.
Liu, Z., Wei, P., Qi, Y., et al., 2023. High stretchable and self-healing nanocellulose-poly(acrylic acid) composite hydrogels for sustainable $CO_2$ shutoff. Carbohydr. Polym. 311, 120759. https://doi.org/10.1016/j.carbpol.2023.120759.
Lu, J., Yuan, M., Di, X., et al., 2024. Fast, non-carbonized, ambient-drying PVA/CNF@GO foam: Towards super-broadband microwave absorption and structural strength enhancement in aramid honeycomb. Chem. Eng. J. 489, 151385. https://doi.org/10.1016/j.cej.2024.151385.
Lyu, J., Chen, H., Luo, J., et al., 2024. Shape memory and hemostatic silk-laponite scaffold for alveolar bone regeneration after tooth extraction trauma. Int. J. Biol. Macromol. 260, 129454. https://doi.org/10.1016/j.ijbiomac.2024.129454.
Mahdavinia, G.R., Mousanezhad, S., Hosseinzadeh, H., et al., 2016. Magnetic hydrogel beads based on PVA/sodium alginate/laponite RD and studying their BSA adsorption. Carbohydr. Polym. 147, 379–391. https://doi.org/10.1016/j.carbpol.2016.04.024.
Mahdavinia, G.R., Soleymani, M., Sabzi, M., et al., 2017. Novel magnetic polyvinyl alcohol/laponite RD nanocomposite hydrogels for efficient removal of methylene blue. J. Environ. Chem. Eng. 5 (3), 2617–2630. https://doi.org/10.1016/j.jece.2017.05.017.
Maiolo, A.S., Amado, M.N., Gonzalez, J.S., et al., 2012. Development and characterization of poly(vinyl alcohol) based hydrogels for potential use as an articular cartilage replacement. Mater. Sci. Eng. C 32 (6), 1490–1495. https://doi.org/10.1016/j.msec.2012.04.030.
Mancilla, Corzo I.J., Lopes da Fonseca, J.H., Ferman, V., et al., 2024. Optimizing biomaterial inks: A study on the printability of carboxymethyl cellulose-laponite nanocomposite hydrogels and dental pulp stem cells bioprinting. Bioprinting 43, e00358. https://doi.org/10.1016/j.bprint.2024.e00358.
Nasiri, A., Ghaffarkhah, A., Dijvejin, Z.A., et al., 2018. Bridging performance of new eco-friendly lost circulation materials. Petrol. Explor. Dev. 45 (6), 1154–1165. https://doi.org/10.1016/S1876-3804(18)30119-8.
Nezadi, M., Keshvari, H., Shokrolahi, F., et al., 2024. Injectable self-healing hydrogels based on gelatin, quaternized chitosan, and laponite as localized celecoxib delivery system for nucleus pulpous repair. Int. J. Biol. Macromol. 266, 131337. https://doi.org/10.1016/j.ijbiomac.2024.131337.
Ochoa-Cornejo, F., Bobet, A., Johnston, C.T., et al., 2016. Cyclic behavior and pore pressure generation in sands with laponite, a super-plastic nanoparticle. Soil Dynam. Earthq. Eng. 88, 265–279. https://doi.org/10.1016/j.soildyn.2016.06.008.
Prasannan, A., Udomsin, J., Tsai, H.-C., et al., 2020. Robust underwater superoleophobic membranes with bio-inspired carrageenan/laponite multilayers for the effective removal of emulsions, metal ions, and organic dyes from wastewater. Chem. Eng. J. 391, 123585. https://doi.org/10.1016/j.cej.2019.123585.
Qi, Y., Al-Mukhtar, M., Alcover, J.F., et al., 1996. Coupling analysis of macroscopic and microscopic behaviour in highly consolidated Na-laponite clays. Appl. Clay Sci. 11 (2), 185–197. https://doi.org/10.1016/S0169-1317(96)00016-6.
Ryu, J., McClements, D.J., 2025. Cellulose reinforcement of plant-based protein hydrogels: Effects of cellulose nanofibers and nanocrystals on physicochemical properties. Food Hydrocoll. 158, 110541. https://doi.org/10.1016/j.foodhyd.2024.110541.
Sajjadi, M., Nasrollahzadeh, M., Sattari, M.R., et al., 2024. Sulfonic acid functionalized cellulose-derived (nano)materials: Synthesis and application. Adv. Colloid Interface Sci. 328, 103158. https://doi.org/10.1016/j.cis.2024.103158.
Šebenik, U., Lapasin, R., Krajnc, M., 2020. Rheology of aqueous dispersions of laponite and TEMPO-oxidized nanofibrillated cellulose. Carbohydr. Polym. 240, 116330. https://doi.org/10.1016/j.carbpol.2020.116330.
Shen, R., Tian, X., Wang, X., et al., 2024. Fibrous cellulose improves the strength and water retention of heat-induced myofibrillar protein gel by microstructure enhancement. Food Hydrocoll. 147, 109437. https://doi.org/10.1016/j.foodhyd.2023.109437.
Silva, J.M., Barud, H.S., Meneguin, A.B., et al., 2019. Inorganic-organic bionanocomposite films based on laponite and cellulose nanofibers (CNF). Appl. Clay Sci. 168, 428–435. https://doi.org/10.1016/j.clay.2018.12.003.
Song, T., Bai, B., Huang, R., et al., 2024. Development and evaluation of lysine-crosslinked re-crosslinkable particle gel for water control in high-temperature reservoirs. J. Mol. Liq. 407, 125133. https://doi.org/10.1016/j.molliq.2024.125133.
Song, Y., Li, Z., Jiang, Z., et al., 2017. Progress and development trend of unconventional oil and gas geological research. Petrol. Explor. Dev. 44 (4), 675–685. https://doi.org/10.1016/S1876-3804(17)30077-0.
Su, X., Lian, Z., Junwei, F., et al., 2019. Lost circulation material for abnormally high temperature and pressure fractured-vuggy carbonate reservoirs in Tazhong block, Tarim Basin, NW China. Petrol. Explor. Dev. 46 (1), 173–180. https://doi.org/10.1016/S1876-3804(19)30017-5.
Sun, B., Wang, Z., Wu, B., et al., 2024. Preparation and adsorption of copper ion properties of anisotropic PVA wood-based hydrogel. J. Forest. Eng. 9 (2), 108–115. https://doi.org/10.1021/acsnano.3c01976.
Supramaniam, J., Low, D.Y.S., Wong, S.K., et al., 2022. Nano-engineered ZnO/CNF-based epoxidized natural rubber with enhanced strength for novel self-healing glove fabrication. Chem. Eng. J. 437, 135440. https://doi.org/10.1016/j.cej.2022.135440.
Tao, X., Zheng, Z., Yu, H., et al., 2024. Internal blocking and bonding to strengthen the mechanical properties and prevent collapse and leakage of fragmented coalbed methane (CBM) reservoirs by cohesive drilling fluids. Geoenergy Sci. Eng. 241, 213136. https://doi.org/10.1016/j.geoen.2024.213136.
Wang, H., Ma, F., Tong, X., et al., 2016. Assessment of global unconventional oil and gas resources. Petrol. Explor. Dev. 43 (6), 925–940. https://doi.org/10.1016/S1876-3804(16)30111-2.
Wei, Y., Sun, X., Sun, Y., et al., 2024. Multibetwork-structured PAM-AG/CNF-MXene triboelectric hydrogels. Ind. Crop. Prod. 216, 118695. https://doi.org/10.1016/j.indcrop.2024.118695.
Wu, H.-R., Li, G.-L., Xu, G.-R., et al., 2024. Emulsion properties and plugging performances of active crude oil enhanced by amphiphilic Janus nanosheets. Pet. Sci. 21 (6), 4141–4152. https://doi.org/10.1016/j.petsci.2024.07.026.
Xu, C., Xie, Z., Kang, Y., et al., 2020. A novel material evaluation method for lost circulation control and formation damage prevention in deep fractured tight reservoir. Energy 210, 118574. https://doi.org/10.1016/j.energy.2020.118574.
Xu, C., Zhang, H., She, J., et al., 2023. Experimental study on fracture plugging effect of irregular-shaped lost circulation materials. Energy 276, 127544. https://doi.org/10.1016/j.energy.2023.127544.
Xu, L., Jiao, G., Huang, Y., et al., 2024a. Laponite nanoparticle-crosslinked carboxymethyl cellulose-based injectable hydrogels with efficient underwater-specific adhesion for rapid hemostasis. Int. J. Biol. Macromol. 255, 128288. https://doi.org/10.1016/j.ijbiomac.2023.128288.
Xu, Y., Liu, S., Xu, S., et al., 2024b. Flexible and flame retardant cotton fiber-reinforced CS/CNF/EP composites for a sensitive fire warning. Chem. Eng. J. 500, 156960. https://doi.org/10.1016/j.cej.2024.156960.
Xu, Z., Sun, W., Liu, J., 2024c. Reducing plug flow effect on measured rheological results of cement-based materials: Image analysis and numerical iteration approach. Constr. Build. Mater. 429. https://doi.org/10.1016/j.conbuildmat.2024.136401.
Yang, Y., He, X., Sun, D., et al., 2023. Pseudointerpenetrating network nanocomposite hydrogel for temporary plugging in fractured reservoirs. Colloids Surf. A Physicochem. Eng. Asp. 656, 130369. https://doi.org/10.1016/j.colsurfa.2022.130369.
Ye, C., Wang, S., Pan, M., 2024. Phosphate adsorption performance of zirconium-calcium synergistically loaded hydrogel. J. Forest. Eng. 5, 101–106. https://doi.org/10.13360/j.issn.2096-1359.202309039.
Yu, C., Dou, X., Meng, L., et al., 2023. Structure, rheological properties, and biocompatibility of laponite® cross-linked starch/polyvinyl alcohol hydrogels. Int. J. Biol. Macromol. 253, 127618. https://doi.org/10.1016/j.ijbiomac.2023.127618.
Zhang, J., Bo, S., Wang, R., et al., 2022. Supramolecular polymer gel lubricant with excellent mechanical stability and tribological performances. ACS Appl. Mater. Interfaces 14 (40), 45934–45944. https://doi.org/10.1021/acsami.2c14306.
Zhao, L., Chang, Z., Guo, B., et al., 2024. Robust, stretchable bioelectronic interfaces for cardiac pacing enabled by interfacial transfer of laser-induced graphene via water-response, nonswellable PVA gels. Biosens. Bioelectron. 261, 116453. https://doi.org/10.1016/j.bios.2024.116453.
Zhao, L.Z., Zhou, C.H., Wang, J., et al., 2015. Recent advances in clay mineral-containing nanocomposite hydrogels. Soft Matter 11 (48), 9229–9246. https://doi.org/10.1039/C5SM01277E.
Zheng, C., Hou, Z., Xu, K., et al., 2023. Preparation and rheological properties of acrylamide-based penta-polymer for ultra-high temperature fracturing fluid. Colloids Surf. A Physicochem. Eng. Asp. 670, 131386. https://doi.org/10.1016/j.colsurfa.2023.131386.
Zheng, L., Wei, P., Zhang, Z., et al., 2017. Joint exploration and development: A self-salvation road to sustainable development of unconventional oil and gas resources. Nat. Gas. Ind. B 4 (6), 477–490. https://doi.org/10.1016/j.ngib.2017.09.010.
Zhou, Q., Luo, Z., Fu, H., et al., 2024. Research and application progress of temporary plugging agent for acidification fracturing: A review. Geoenergy Sci. Eng., 213600 https://doi.org/10.1016/j.geoen.2024.213600.
Zhu, M., Wang, Z., Zhou, H., et al., 2024. Advances in cellulose nanofiber hydrogels for self-powered wearable pressure sensors. J. Forest. Eng. 6, 114–123. https://doi.org/10.1016/j.nanoen.2024.109790.